

# Muon $g-2$ and a type-X two Higgs doublet scenario: some studies in high-scale validity

Atri Dey,<sup>a</sup> Jayita Lahiri,<sup>b</sup> Biswarup Mukhopadhyaya,<sup>c</sup>

<sup>a</sup>*Regional Centre for Accelerator-based Particle Physics, Harish-Chandra Research Institute, HBNI, Chhatnag Road, Jhansi, Allahabad - 211 019, India*

<sup>b</sup>*Department of Physics, Indian Institute of Technology Guwahati, North Guwahati, Assam - 781039, India*

<sup>c</sup>*Department of Physical Sciences, Indian Institute of Science Education and Research Kolkata, Mohanpur - 741246, India*

*E-mail:* [atridey@hri.res.in](mailto:atridey@hri.res.in), [jayitalahiri@rnd.iitg.ac.in](mailto:jayitalahiri@rnd.iitg.ac.in),  
[biswarup@iiserkol.ac.in](mailto:biswarup@iiserkol.ac.in)

**ABSTRACT:** We study the high-scale validity of a Type-X two Higgs doublet scenario which provides an explanation of the observed value of muon ( $g - 2$ ). This region admits of a pseudoscalar physical state, which is well below the observed 125-GeV scalar in mass. A second neutral scalar particle can be both above and below 125 GeV in such a scenario. Admissible regions in the parameter space are obtained by using the most recent data on muon ( $g - 2$ ), theoretical constraints such as low-scale perturbativity and vacuum stability, and also all experimental constraints, including the available LHC results. Among other things, both the aforesaid orders of CP-even neutral scalar masses are included in our benchmark studies. Two-loop renormalisation group equations are used to predict the values of various couplings at high scales, and the regions in the space spanned by low-scale parameters, which retain perturbative unitarity as well as vacuum stability upto various scales are identified. We thus conclude that such a scenario, while successfully explaining the observed muon ( $g - 2$ ), can be valid upto energy scales ranging from  $10^4$  GeV to the Planck scale, thus opening up directions of thought on its ultraviolet completion.

---

## Contents

<b>1</b>	<b>Introduction</b>	<b>2</b>
<b>2</b>	<b>Type-X two Higgs Doublet Model</b>	<b>3</b>
<b>3</b>	<b>Explanation of <math>g_\mu - 2</math></b>	<b>6</b>
<b>4</b>	<b>Other constraints on model parameters</b>	<b>9</b>
4.1	Constraints from electroweak precision observables	9
4.2	Theoretical constraints	10
4.3	Constraints from the direct search at colliders	12
4.4	Allowed parameter space	15
<b>5</b>	<b>The running of various couplings</b>	<b>19</b>
5.1	The Renormalization Group Equations(RGEs)	19
5.2	Coupling trajectories and inference drawn from them	21
<b>6</b>	<b>Allowed regions with various cut-off scales</b>	<b>27</b>
<b>7</b>	<b>Conclusion</b>	<b>39</b>
<b>8</b>	<b>Acknowledgements</b>	<b>40</b>

---

## 1 Introduction

It is often speculated that the spontaneous symmetry-breaking sector of the electroweak theory may include additional ingredients, over and above the single complex Higgs doublet postulated in the ‘minimal’ original framework. The simplest and most obvious extension is a scenario with two complex scalar doublets. The spectrum of physical fields in such a case, after the absorption of three Goldstone bosons, consists of two CP-odd neutral scalars, one CP-even neutral scalar and a pair of mutually conjugate charged scalar bosons. While the doublets can both acquire vacuum expectation values (VEV) in such a scenario, the Yukawa couplings to fermions are more model-specific, depending on the various possibilities restricted by the principle of natural flavour conservation. Various phenomenological features of a two Higgs doublet model (2HDM) are accordingly decided.

A scenario of particular interest is the Type-X 2HDM where one of the scalar doublets couples only to quarks, and the other, to leptons. The doublet that couples to quarks dominates the mass eigenstate corresponding to the 125-GeV scalar that has been experimentally discovered. We are concerned with this kind of a theory in the present work.

A rather striking consequence of a Type-X 2HDM is that it admits of scalar physical states considerably lighter than 125 GeV, consistently with all experimental observations so far. In particular, the neutral pseudoscalar here can be well below 100 GeV. This is worthy of special mention because such a light pseudoscalar can mediate contributions to the muon anomalous magnetic moment, leading to a closer agreement with the experimental observation [1–3]. Keeping this in mind, the region of the parameter space answering to such a light pseudoscalar has been investigated from various angles in recent times, including its implications for the LHC [4–14].

For experimental detectability, one largely depends on the pair-production of the light pseudoscalar in the decay of the 125-GeV scalar, a process whose branching ratio (and hence its parameter space) is restricted by the four-lepton branching ratio. This is because the pseudoscalar in the alignment limit is dominated by the doublet giving masses to leptons. Also, the 125-GeV particle can be either the lighter or the heavier of the two CP-even neutral scalars. A deciding factor here is  $\sin(\beta - \alpha)$ , where  $\alpha$  is the mixing angle between the real parts of the two doublets, and  $\tan \beta$  is the ratio of the two VEVs. In addition, wrong-sign Yukawa coupling is an allowed feature of a Type-X 2HDM of the kind we are interested in. The sign of  $\sin(\beta - \alpha)$  and the function  $\tan \beta$  are of primary importance in this context. The parameter  $\tan \beta$  plays crucial role throughout our analysis. This is especially because the closest agreement with the experimental value of muon  $g - 2$  (henceforth to be called  $g_\mu - 2$ ) can be achieved for large ( $\gtrsim 20$ )  $\tan \beta$ . The viability of such  $\tan \beta$  in this scenario, from both phenomenological and theoretical angles, is therefore worth studying.

The question we ask here is: can the aforesaid aspects of low-energy phenomenology provide any hint of the UV completion of this scenario? If so, then not only does the muon anomalous magnetic moment get related to high-scale physics, but we also build towards some insights into features such as the signs of Yukawa interactions at low energy. With this in view, we have undertaken a detailed study of the high-scale behavior of

the various quartic couplings in the scalar potential of the Type-X 2HDM. Limits on its high-scale validity then arise from vacuum stability, perturbativity and unitarity of the couplings. This exercise has been carried out across various regions of the parameter space, including both right-and wrong-sign Yukawa interaction regions, where the muon anomalous magnetic moment is better explained, and all other theoretical and experimental constraints are satisfied. We make use of two-loop renormalisation group (RG) equations. However, it is demonstrated in some illustrative cases that the difference in the results is not qualitative, as compared to those obtained with one-loop RGs. Therefore, the explanation of the allowed regions of the parameter space corresponding to various levels of high-scale validity has been often given by referring to the one-loop RGs where the effects of different parameters of the theory are more transparent.

The plan of this work is as follows. In Section 2, we discuss the Type-X two Higgs doublet model and its various aspects relevant for our analysis. Section 3 summarises the implications of the observed  $g_\mu - 2$  for this specific model. We discuss various theoretical and experimental constraints on this model and the allowed parameter space in Section 4. In Section 5, we study the renormalization group evolution of various couplings for a few benchmarks. We next identify in Section 6, the regions of parameter space which are valid upto various high scales and are also interesting from the perspective of the anomalous magnetic moment of muon as well as relevant collider searches. This way we try to explore the validity of Type-X 2HDM as a UV-complete theory. Finally, we conclude our analysis in Section 7.

## 2 Type-X two Higgs Doublet Model

The most general scalar potential involving two scalar doublets with hypercharge  $Y = 1$ , under the assumption of a softly broken discrete  $Z_2$  symmetry, is given by [15]

$$\begin{aligned} V = & m_{11}^2(\Phi_1^\dagger\Phi_1) + m_{22}^2(\Phi_2^\dagger\Phi_2) - \left[ m_{12}^2(\Phi_1^\dagger\Phi_2 + \text{h.c.}) \right] \\ & + \frac{\lambda_1}{2}(\Phi_1^\dagger\Phi_1)^2 + \frac{\lambda_2}{2}(\Phi_2^\dagger\Phi_2)^2 + \lambda_3(\Phi_1^\dagger\Phi_1)(\Phi_2^\dagger\Phi_2) + \lambda_4(\Phi_1^\dagger\Phi_2)(\Phi_2^\dagger\Phi_1) \\ & + \left[ \frac{\lambda_5}{2}(\Phi_1^\dagger\Phi_2)^2 + \text{h.c.} \right]. \end{aligned} \quad (2.1)$$

We assume CP-conservation, in which case all  $\lambda_i$ 's and  $m_{12}^2$  are real.

The two complex Higgs doublets with hypercharge  $Y = 1$  can be written as

$$\Phi_1 = \begin{pmatrix} \phi_1^+ \\ \frac{1}{\sqrt{2}}(v_1 + \phi_1^0 + ia_1) \end{pmatrix}, \quad \Phi_2 = \begin{pmatrix} \phi_2^+ \\ \frac{1}{\sqrt{2}}(v_2 + \phi_2^0 + ia_2) \end{pmatrix}. \quad (2.2)$$

Where  $v_1$  and  $v_2$  are the vacuum expectation values with  $v^2 = v_1^2 + v_2^2 = (246 \text{ GeV})^2$  and  $\tan\beta = v_2/v_1$ . After electroweak symmetry breaking, we obtain five physical states, two neutral CP-even scalars, the lighter of which will be called  $h$ , and the heavier  $H$ , one neutral pseudoscalar  $A$ , and a pair of charged scalars  $H^\pm$ .

In Type-X 2HDM the Yukawa interactions can be given as

$$-\mathcal{L}_{Yukawa} = Y_{u2} \bar{Q}_L \tilde{\Phi}_2 u_R + Y_{d2} \bar{Q}_L \Phi_2 d_R + Y_{\ell 1} \bar{L}_L \Phi_1 e_R + \text{h.c.} \quad (2.3)$$

in which  $Q_L^T = (u_L, d_L)$ ,  $L_L^T = (\nu_L, l_L)$ , and  $\tilde{\Phi}_{1,2} = i\tau_2 \Phi_{1,2}^*$ .  $Y_{u2}$ ,  $Y_{d2}$  and  $Y_{\ell 1}$  are the couplings of the up, down quarks and leptons with the two doublets, family indices are suppressed.

The factors by which the Standard Model(SM) Higgs interaction strengths need to be scaled to obtain the neutral scalar Yukawa couplings, are

$$\begin{aligned} y_h^{f_i} &= [\sin(\beta - \alpha) + \cos(\beta - \alpha)\kappa_f], \\ y_H^{f_i} &= [\cos(\beta - \alpha) - \sin(\beta - \alpha)\kappa_f], \\ y_A^{f_i} &= -i\kappa_f \text{ (for u)}, \quad y_A^{f_i} = i\kappa_f \text{ (for d, } \ell), \\ &\text{with } \kappa_\ell \equiv -\tan \beta, \quad \kappa_u = \kappa_d \equiv 1/\tan \beta. \end{aligned} \quad (2.4)$$

The corresponding charged Higgs Yukawa couplings are:

$$\mathcal{L}_Y = -\frac{\sqrt{2}}{v} H^+ \left\{ \bar{u}_i [\kappa_d (V_{CKM})_{ij} m_{dj} P_R - \kappa_u m_{ui} (V_{CKM})_{ij} P_L] d_j + \kappa_\ell \bar{\nu} m_\ell P_R \ell \right\} + \text{h.c.}, \quad (2.5)$$

in which  $i, j = 1, 2, 3$ .

The couplings of gauge boson pairs with the neutral scalars are given by

$$y_h^V = \sin(\beta - \alpha) \times g_{SM}^V, \quad y_H^V = \cos(\beta - \alpha) \times g_{SM}^V, \quad (2.6)$$

Where  $V$  denotes  $W$  or  $Z$  and  $g_{SM}^V$  is the coupling strength of the SM Higgs with a gauge boson pair.

Furthermore, Yukawa couplings here may or may not have the same sign as in the SM case [16],

$$\begin{aligned} y_h^{f_i} \times y_h^V &> 0 \text{ for SM-like coupling or right-sign(RS)}, \\ y_h^{f_i} \times y_h^V &< 0 \text{ for wrong-sign(WS)}. \end{aligned} \quad (2.7)$$

This can happen, for example, for down-type Yukawa couplings in Type II 2HDM [16] as well. However, in Type-X 2HDM the wrong-sign Yukawa coupling can arise in the lepton Yukawa sector alone, unless one allows  $\tan \beta < 1$ . In case of the SM-like coupling, the 125-GeV Higgs couplings are very close to those in the SM, which is the so-called alignment limit. Now in the wrong-sign regime, the absolute values of  $y_h^\ell$  and  $y_h^V$  should still be close to unity because of the restrictions of 125-GeV Higgs signal data [17, 18]. Moreover, there are two scenarios, a) The lightest CP-even scalar  $h$  is SM-like ie.  $m_h = m_{h_{SM}} = 125$  GeV, we call this **Scenario 1** and b) when the heavier CP-even scalar  $H$  is SM-like, ie.  $m_H = m_{h_{SM}} = 125$  GeV, we call this **Scenario 2**. Both scenario 1 and 2 can in principle lead to right-sign or wrong-sign of Yukawa coupling depending on the conditions stated in Equation 2.7.

Let us first consider Scenario 1 in the right- and wrong-sign regions. In scenario 1, the 125-GeV Higgs couplings are:

$$y_h^\ell = \sin(\beta - \alpha) - \cos(\beta - \alpha) \tan \beta, \quad y_h^V \simeq \sin(\beta - \alpha)$$

In the alignment limit  $|\sin(\beta - \alpha)| \approx 1$ . The following possibilities emerge depending on the sign of  $\sin(\beta - \alpha)$  and range of  $\tan \beta$ .

- For  $\sin(\beta - \alpha) < 0$ ,  $\cos(\beta - \alpha) > 0$ ,  $y_h^\ell$  takes the form  $-(1 + \epsilon)$ .  $y_h^\ell \times y_h^V > 0$  and it corresponds to right-sign region.
- On the other hand, for  $\sin(\beta - \alpha) > 0$ ,  $\cos(\beta - \alpha) > 0$ ,  $y_h^\ell$  takes the form  $(1 - \epsilon)$ . This case also corresponds to the right-sign region.
- When  $\sin(\beta - \alpha) > 0$  and  $\cos(\beta - \alpha) > 0$  and  $\tan \beta \gtrsim 10$ ,  $y_h^\ell$  becomes negative and  $y_h^\ell \times y_h^V < 0$ . This scenario gives rise to wrong-sign lepton-Yukawa coupling.

Having discussed the coupling structure in Scenario 1, we will now explore the same for Scenario 2. In this case, the heavier CP-even Higgs is the observed 125 GeV Higgs ie.  $m_H = 125$  GeV. Here the couplings of  $H$  with the leptons and gauge bosons take the following forms.

$$y_H^\ell = \cos(\beta - \alpha) + \sin(\beta - \alpha) \tan \beta, \quad y_H^V \simeq \cos(\beta - \alpha)$$

In the alignment limit,  $|\sin(\beta - \alpha)| \ll 1$ . The sign of  $\sin(\beta - \alpha)$  and ranges of  $\tan \beta$  in this case will give rise to the following conditions.

- For  $\sin(\beta - \alpha) > 0$ ,  $\cos(\beta - \alpha) > 0$ ,  $y_H^\ell$  takes the form  $(1 + \epsilon)$  and  $y_H^\ell \times y_H^V > 0$ . Therefore this case corresponds to the right-sign region.
- On the other hand, for  $\sin(\beta - \alpha) < 0$ ,  $\cos(\beta - \alpha) > 0$ ,  $y_H^\ell$  takes the form  $(1 - \epsilon)$ ,  $y_H^\ell \times y_H^V > 0$ . Hence this region also gives rise to right-sign lepton-Yukawa coupling.
- When  $\sin(\beta - \alpha) < 0$  and  $\cos(\beta - \alpha) > 0$  and  $\tan \beta \gtrsim 10$ ,  $y_H^\ell$  becomes negative and  $y_H^\ell \times y_H^V < 0$ . In this scenario, wrong-sign condition is satisfied.

Throughout the discussion concerning Scenario 1 and Scenario 2,  $\epsilon$  is assumed to be an extremely small positive quantity. One should note that  $\tan \beta (\gtrsim 10)$  in the right-sign region will give rise to Yukawa scale factors widely differing from unity (therefore disfavored by the Higgs signal strength data), unless  $|\sin(\beta - \alpha)|$  (Scenario 1) or  $|\cos(\beta - \alpha)|$  (Scenario 2) is very close to 1. Notably,  $\cos(\beta - \alpha)$  is kept positive in all the above cases, since the sign of the Yukawa interactions are unambiguously decided by  $(\beta - \alpha)$  lying in two of the four quadrants. The required ranges of  $\tan \beta$  are not altered by such quadrant choice.

The main motivation of the present study is to explore the possibility of having a light ( $\lesssim 100$  GeV) pseudoscalar in Type-X 2HDM, which makes it easier to match the observed value of  $g_\mu - 2$ . We will see in the following section that large  $\tan \beta$  regions will be favored from this particular requirement. There will be further overlap or tension between various theoretical and experimental constraints on the model parameter space. These are decisive in understanding the high-scale validity of the scenario, which is our ultimate purpose here.

### 3 Explanation of $g_\mu - 2$

The anomalous magnetic moment of muon is an early triumph of quantum field theory. In today's context, the long-standing discrepancy between SM prediction and experimental observation [19] hints towards new physics. The recent result from Fermilab [2, 3] has strengthened this disagreement further. The future E34 experiment at J-PARC [20] may shed new light on this tension between theory and experiment.

The effect of loop corrections are usually parameterized in terms of  $a_\mu = \frac{g_\mu - 2}{2}$ . The SM contributions to  $a_\mu = \frac{g_\mu - 2}{2}$  have been extensively studied [21–43], the most recent estimate [44] being

$$a_\mu^{SM} = 116591810(43) \times 10^{-11} \quad (3.1)$$

While the most recent experimental bound is obtained by combining the Fermilab data(2021) [2, 3] and earlier BNL(2006) data [1].

$$a_\mu^{exp} = 116592040(54) \times 10^{-11} \quad (3.2)$$

This may be contrasted with the earlier limits from BNL data [1].

$$a_\mu^{exp-BNL} = 116592089(63) \times 10^{-11} \quad (3.3)$$

Thus there is approximately  $4.2\sigma$  discrepancy when one uses the combined experimental result (Equation 3.2).

$$\Delta a_\mu = a_\mu^{exp} - a_\mu^{SM} = 251(59) \times 10^{-11} \quad (3.4)$$

On the other hand, a discrepancy at the level of  $3.7\sigma$  is seen, if one uses only the BNL data (Equation 3.3).

$$\Delta a_\mu^{BNL} = a_\mu^{exp-BNL} - a_\mu^{SM} = 279(76) \times 10^{-11} \quad (3.5)$$

We consider one loop as well as two loop Bar-Zee type contribution to  $\Delta a_\mu$  in Type-X 2HDM. It has been shown in earlier works [45, 46], that the two-loop Bar-Zee diagrams dominate over the one-loop contributions, both of which are shown in figures 1-4. Although the two loop diagrams suffer from a loop suppression factor, they also have an enhancement factor of  $\frac{M^2}{m_\mu^2}$ , where  $M$  is the mass of the heavy particle running in the loop namely,  $t, b, \tau, H^\pm, W^\pm$  (see Figure 2). One should note that in Type-X 2HDM, the contribution from the  $\tau$  loop gets additional enhancement factor from the  $\tau$  coupling with pseudoscalar( $A$ ) in the large  $\tan\beta$  region. The enhancement factor in general dominates over the aforementioned loop suppression. The diagram involving  $W^\pm$  in the loop (Figure 2 bottom), will have negligible contribution due to suppression in the coupling between  $W^\pm$  bosons and the non-standard CP-even Higgs in the alignment limit. We also consider the Bar-Zee diagrams where charged Higgs replaces the neutral Higgs and also  $W^\pm$  substitutes the internal  $\gamma$  (see Figure 3 and 4). The contribution from these diagrams can be sizable in some regions of the parameter space [46].

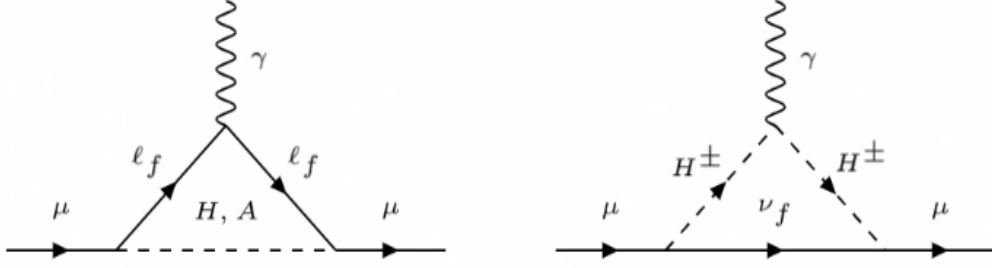


**Figure 1.** Non-standard contribution to  $\Delta a_\mu$  at one-loop.

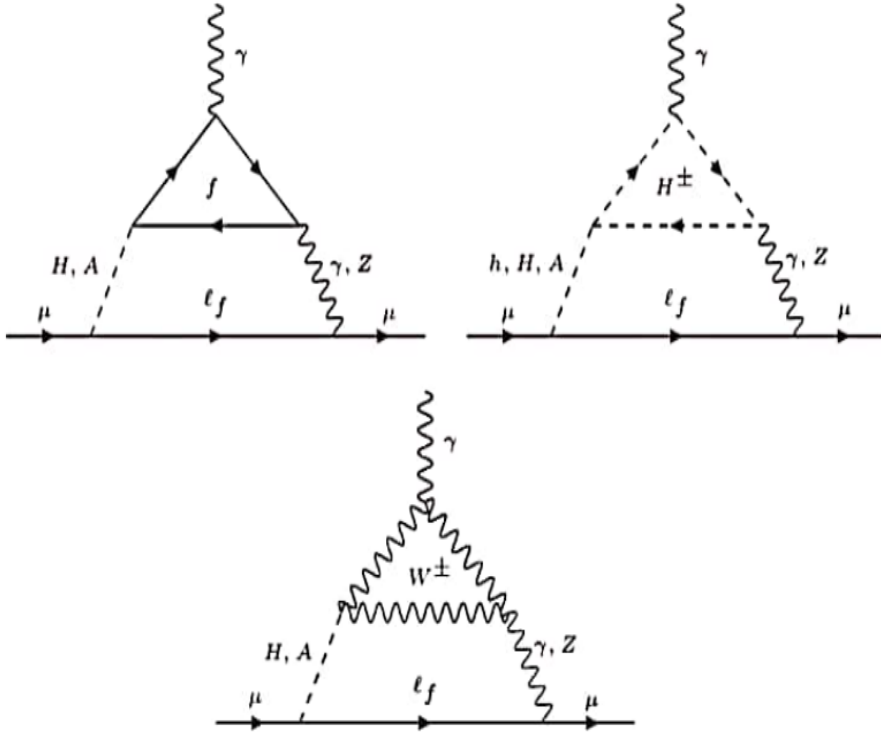


**Figure 2.** Non-standard contribution to  $\Delta a_\mu$  from two-loop Bar-Zee diagrams with internal  $\gamma/Z$ .

In order to obtain updated constraints on  $\Delta a_\mu$ , we have calculated afresh the contributions from all the aforementioned diagrams following [45, 46]. The resulting constraints on the  $m_A - \tan \beta$  plane is shown in Figure 5.  $3\sigma$  upper and lower bound on the experimentally observed central value of  $\Delta a_\mu$  have been used in the scan. While such scans have been carried out earlier [47, 48], we have (a) used the most recent constraints and (b) have used all new physics diagrams exhaustively in our analysis.

In Figure 5, the yellowish interior corresponds to the region that satisfies constraints



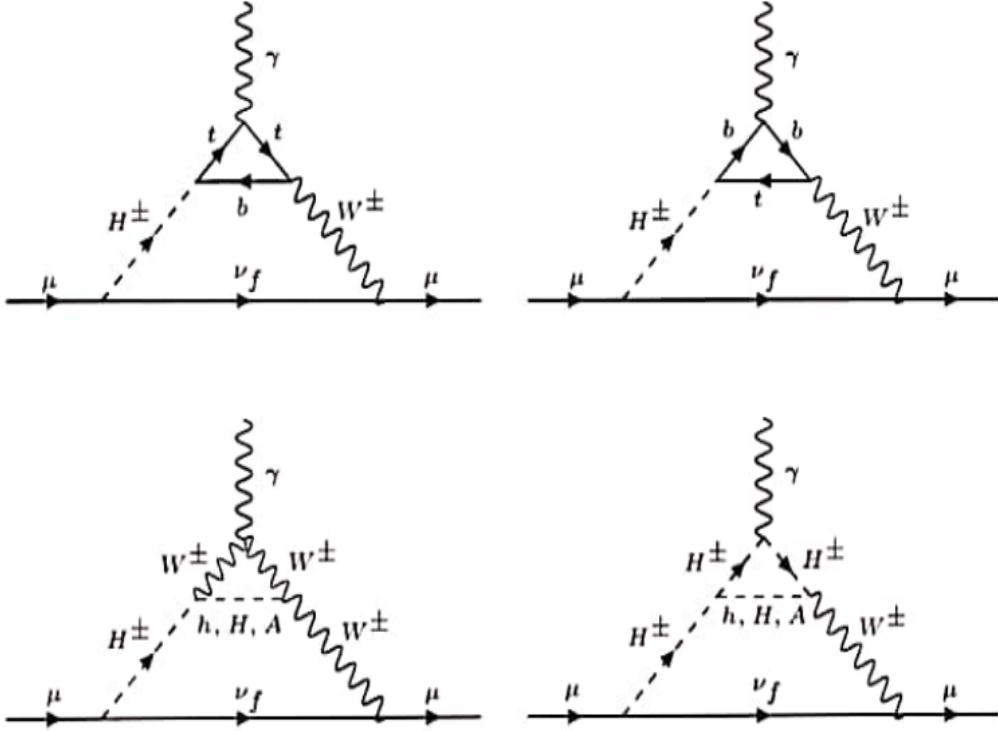


**Figure 3.** Non-standard contribution to  $\Delta a_\mu$  from two-loop Bar-Zee diagrams with internal  $W^\pm$  and  $H^\pm$ . Cross-diagrams with  $H^\pm$  and  $W^\pm$  interchanged are also considered.

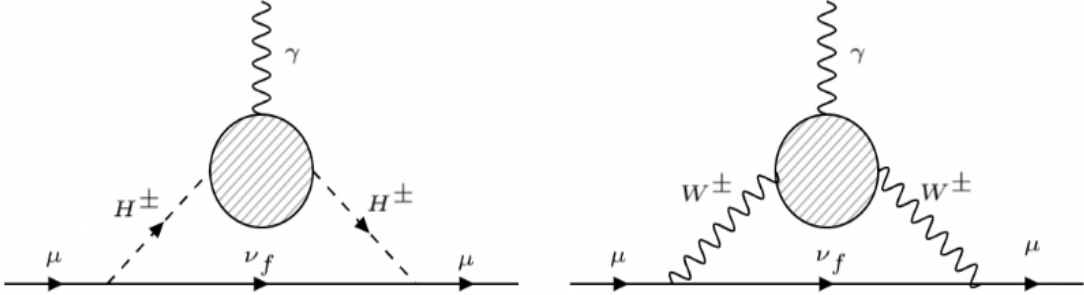


**Figure 4.** Same as in Figure 3, but with both internal lines  $H^\pm H^\pm$  and  $W^\pm W^\pm$ .

coming from a combination of the BNL and Fermilab data. The red bands on both sides of this region, denote the additional regions which are allowed at the  $3\sigma$  level before Fermilab data came into existence. The red band on the lower side is consistent even when the new data are included, so long as one allows experimental values to be undersaturated by Type-X 2HDM. On the other hand, points in the upper red band overshoots the  $3\sigma$  limit arising from the combined data, and therefore, may be taken to be in conflict with the

most recent experiments.

It is clear that a low mass pseudoscalar with an enhanced coupling to the  $\tau$  leptons will give significant contribution to  $\Delta a_\mu$  (see Figure 2(top left)), especially for large  $\tan\beta$ . Overall, low  $m_A$  and large  $\tan\beta$  region is favored in the light of  $g_\mu - 2$  data in our model. In this work we are interested to know the high-scale behavior of this particular region of parameter space. Before exploring the high-scale validity of this region of the parameter space, we would like to consider the other important theoretical as well as experimental constraints on such a scenario.

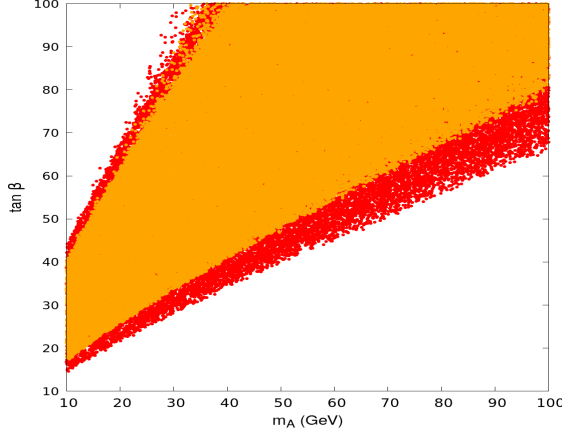


**Figure 5.** The allowed region in  $m_A - \tan\beta$  plane from  $g_\mu - 2$  data at  $3\sigma$  level. The limits have been obtained by marginalizing over all other parameters of the 2HDM, except the mass of one of the neutral CP-even scalars is set at 125 GeV. The yellowish interior corresponds to the combined constraints from older [1] and recent data [2, 3], while the red regions on both sides show the additional regions allowed when only the older data are used.

## 4 Other constraints on model parameters

### 4.1 Constraints from electroweak precision observables

The custodial SU(2) is a symmetry of the tree-level 2HDM potential and can be broken at the loop level due to corrections to weak boson masses as well as weak couplings by extra scalars in 2HDM. Electroweak precision measurements of the oblique parameters, have been performed by the Gfitter group [49]. This restricts the mass difference between the charged scalar and the non-standard CP-even scalar  $|\Delta m| = |m_{h/H} - m_{H^\pm}|$ , depending on  $m_A$  and values of  $m_{H^\pm}$  [47]. The status of two Higgs doublet models in the light of global electroweak data has been presented in [50]. The allowed parameter space in  $m_A - \Delta m$  plane is shown in Figure 6 with color-coded representation of  $m_{H^\pm}$ . We mention here that we have considered the elliptic contour in the  $S - T$  plane computed with  $U$  as a free parameter. This choice leaves us with a less constrained parameter space than the scenario when  $U$  is fixed at 0.

It can be seen from Figure 6 that, in the pseudoscalar mass range of our interest ( $m_A \lesssim 100$  GeV), when  $m_{h/H} < m_{H^\pm}$ , it is possible to get upto  $|\Delta m| \lesssim 50$  GeV, only in

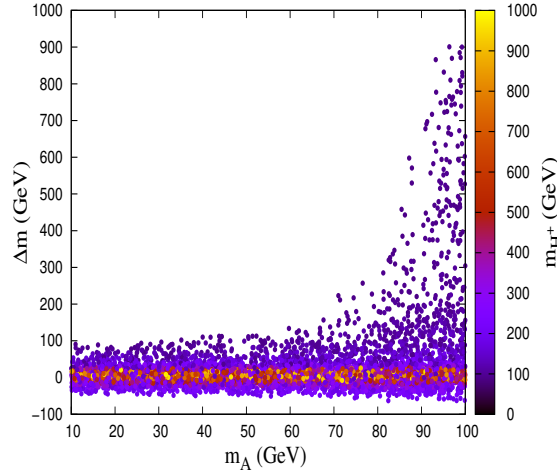


**Figure 6.** Allowed parameter space in  $m_A - \Delta m$  plane consistent with the observed values of  $S, T, U$  parameters at  $3\sigma$ . The charged Higgs mass  $m_{H^\pm}$  has been shown here as the third axis.

the limit of low  $m_{H^\pm}$  ( $\lesssim 200$  GeV). Notably, large positive  $\Delta m$  (upto a TeV or so) can be allowed when  $A$  and  $H^\pm$  are closely degenerate.

#### 4.2 Theoretical constraints

Theoretical constraints include perturbativity, unitarity and vacuum stability conditions at the electroweak scale. Effects of these constraints on various 2HDMs have been studied in detail in earlier works [51–53]. It has been pointed out that large separation between  $m_A$  and  $m_{H^\pm}$  is disfavored from the requirement of vacuum stability and perturbativity. We concentrate on the low  $m_A$  region and therefore it is crucial to look at the allowed upper limit on  $m_{H^\pm}$  in this scenario.

- **perturbativity and unitarity:** If 2HDM is a perturbative quantum field theory at a given scale, it would imply, all quartic couplings  $C_{H_i H_j H_k H_l} < 4\pi$  and all Yukawa couplings  $Y_j < \sqrt{4\pi}$ . Further, unitarity bound on the tree level scattering amplitude of the Higgses and longitudinal parts of EW gauge bosons put an upper bound on the eigenvalues  $|a_i| \leq 8\pi$  of the  $2 \rightarrow 2$  scattering matrices [54, 55].

The physical masses can be written as a function of the quartic couplings in the following manner.

$$m_A^2 = \frac{m_{12}^2}{\sin \beta \cos \beta} - \lambda_5 v^2 \quad (4.1)$$

$$m_{H^\pm}^2 \approx m_A^2 + \frac{1}{2} v^2 (\lambda_5 - \lambda_4) \quad (4.2)$$

It is clear from Equation 4.2 that  $m_{H^\pm}^2 - m_A^2$  is proportional to  $\lambda_5 - \lambda_4$  which should be less than  $\lambda_3 + \sqrt{\lambda_1 \lambda_2}$  from the requirement of vacuum stability (see Equation 4.6). Therefore these conditions along with the requirement of perturbativity ie.  $C_{H_i H_j H_k H_l} < 4\pi$  puts an upper limit on the mass square difference  $m_{H^\pm}^2 - m_A^2$ .

In what follows, we translate these constraints into those of the parameter space for both right- and wrong-sign Yukawa couplings. With this in view, we first express the quartic couplings in terms of physical masses and mixing angles.

$$\begin{aligned}
\lambda_1 &= \frac{m_H^2 \cos^2 \alpha + m_h^2 \sin^2 \alpha - m_{12}^2 \tan \beta}{v^2 \cos^2 \beta}, \\
\lambda_2 &= \frac{m_H^2 \sin^2 \alpha + m_h^2 \cos^2 \alpha - m_{12}^2 \cot \beta}{v^2 \sin^2 \beta}, \\
\lambda_3 &= \frac{(m_H^2 - m_h^2) \cos \alpha \sin \alpha + 2m_{H\pm}^2 \sin \beta \cos \beta - m_{12}^2}{v^2 \sin \beta \cos \beta}, \\
\lambda_4 &= \frac{(m_A^2 - 2m_{H\pm}^2) \sin \beta \cos \beta + m_{12}^2}{v^2 \sin \beta \cos \beta}, \\
\lambda_5 &= \frac{m_{12}^2 - m_A^2 \sin \beta \cos \beta}{v^2 \sin \beta \cos \beta}.
\end{aligned} \tag{4.3}$$

It is clear from the expression of  $\lambda_1$  in Equation 4.3 that, to have it in the perturbative limit, the soft  $Z_2$  breaking parameter  $m_{12}^2 \approx \frac{m_H^2}{\tan \beta}$ . Also the perturbativity condition of the quartic couplings  $\lambda_4$  and  $\lambda_5$  implies  $m_{H\pm}^2 - m_A^2 < 4\pi v^2$  which translates to the limit  $m_{H\pm} \lesssim 870$  GeV for very low  $m_A$ .

• **Vacuum stability:** Vacuum stability demands there can exist no direction in the field space in which  $\mathcal{V} \rightarrow -\infty$ . This implies the following conditions on the quartic couplings of the Higgs potential [56–58].

$$\lambda_{1,2} > 0, \tag{4.4}$$

$$\lambda_3 > -\sqrt{\lambda_1 \lambda_2} \tag{4.5}$$

$$|\lambda_5| < \lambda_3 + \lambda_4 + \sqrt{\lambda_1 \lambda_2} \tag{4.6}$$

The last condition in Equation 4.6 can be rewritten as  $\lambda_3 + \lambda_4 - \lambda_5 > -\sqrt{\lambda_1 \lambda_2}$  for  $m_H > m_A$ . One of the key features to note is that, the upper limits on the heavy Higgs masses show quite different behaviors in the right-sign and wrong-sign limit of the Yukawa couplings [59]. The light-Higgs Yukawa couplings for leptons  $y_h^\ell$  in Type-X 2HDM can be expressed as

$$y_h^\ell = -\frac{\sin \alpha}{\cos \beta} \equiv \sin(\beta - \alpha) - \tan \beta \cos(\beta - \alpha). \tag{4.7}$$

The 125 GeV-Higgs boson couplings are experimentally found to be very much SM-like, implying, in particular,  $|\sin(\beta - \alpha)| \simeq 1$  and  $|y_h^\ell| \approx 1$ . This can be achieved when  $\tan \beta \cos(\beta - \alpha) \approx 0$  (leading to the right-sign lepton coupling  $y_h^\ell \approx +1$ ), or in the large  $\tan \beta$  limit with  $\tan \beta \cos(\beta - \alpha) \approx 2$  (leading to the wrong-sign coupling  $y_h^\ell \approx -1$ ). Using the Equations 4.7 and 4.3, one finds

$$\lambda_3 + \lambda_4 - \lambda_5 = \frac{2m_A^2 + y_h^\ell \sin(\beta - \alpha)m_h^2 - (\sin^2(\beta - \alpha) + y_h^\ell \sin(\beta - \alpha))m_H^2}{v^2} + \mathcal{O}\left(\frac{1}{\tan^2 \beta}\right) \tag{4.8}$$

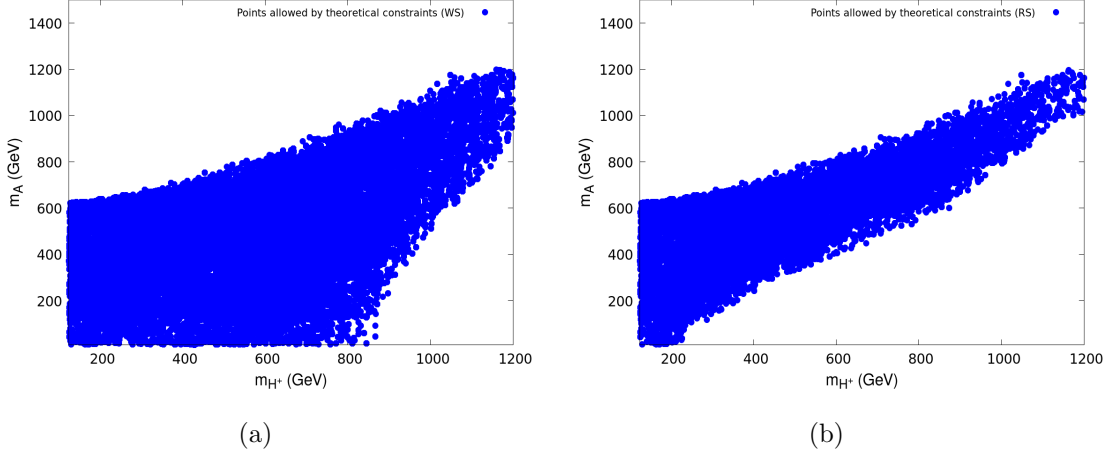


**Figure 7.** Allowed parameter space in  $m_{H^\pm} - m_A$  plane consistent with theoretical bounds in the (a) WS and (b) RS case.

in the large  $\tan \beta$  limit. Now, in the right-sign case ( $y_h^\ell \sin(\beta - \alpha) \rightarrow +1$ ), we have

$$2 \frac{m_H^2}{v^2} < \sqrt{0.26 \times 4\pi} + \frac{2m_A^2 + m_h^2}{v^2} \quad (4.9)$$

which puts a strong upper bound,  $m_H \lesssim 250$  GeV for low  $m_A$ , which is consistent with [47]. On the other hand, in the wrong-sign limit ( $y_h^\ell \sin(\beta - \alpha) \rightarrow -1$ ),  $m_H$  can be arbitrarily large with the condition  $\sin^2(\beta - \alpha) + y_h^\ell \sin(\beta - \alpha) \approx 0$  being trivially satisfied in the alignment limit. These particular properties of wrong-sign and right-sign regions can be seen from Figures 7(a) and (b).

### 4.3 Constraints from the direct search at colliders

#### • LEP data:

The earliest collider constraint on the masses of charged and neutral scalars came from the LEP experiments [60]. The charged Higgs has been searched for at LEP in the process  $e^+e^- \rightarrow \gamma/Z \rightarrow H^+H^-$  with subsequent decay  $H^\pm \rightarrow \tau^\pm \nu_\tau$ . Direct search at LEP in this channel provides a lower limit on charged Higgs mass  $m_{H^\pm}$  as a function of  $\text{BR}(H^\pm \rightarrow \tau^\pm \nu_\tau)$ . The strongest bound results in  $m_{H^\pm} \gtrsim 90$  GeV [60] at 95% CL., considering  $\text{BR}(H^\pm \rightarrow \tau \nu_\tau \approx 100\%)$ . However, the upper limit varies only mildly with the  $\text{BR}(H^\pm \rightarrow \tau \nu_\tau)$  and therefore is fairly model-independent. On the other hand, another LEP search in the channel  $pp \rightarrow hA \rightarrow 4\tau$  also puts an upper limit on  $\text{BR}(h \rightarrow \tau^+\tau^-) \times \text{BR}(A \rightarrow \tau^+\tau^-) \times R_{hA}$  (mixing between two doublets) for  $m_A + m_h$  upto 200 GeV [61].

#### • LHC data on the SM-like Higgs:

An important constraint comes from the direct search for 125-GeV Higgs decaying into two light pseudoscalar final states when it is kinematically allowed. The upper bound on this branching ratio puts severe constraint on the parameter space of this model. As

$g_\mu - 2$  constraint pushes us to a region tilted towards large  $\tan\beta$  with small  $m_A$ , it can lead to substantial branching fraction in the decay mode  $h_{SM} \rightarrow AA$ , when this particular decay is kinematically allowed ie.  $m_A \lesssim \frac{m_h}{2}$ . At large  $\tan\beta$ , pseudoscalar  $A$  decays to  $\tau^+\tau^-$  pair with  $\gtrsim 99\%$  branching fraction, leaving a small branching fraction ( $\sim 0.35\%$ ) in the  $\mu^+\mu^-$  final state [6, 7, 62, 63]. LHC searches for  $h_{SM} \rightarrow AA$  in the  $4\tau$  or  $2\tau + 2\mu$  final state disfavors a large  $\text{BR}(h_{SM} \rightarrow AA)$ . We impose the most stringent upper limit  $\text{BR}(h_{SM} \rightarrow AA) \lesssim 0.04$ , consistent with the upper bounds provided by the experimental results [64, 64]<sup>1</sup>.

First we consider Scenario 1 ie.  $m_h = 125$  GeV. The partial decay width of Higgs decaying to a pair of pseudoscalars is given by

$$\Gamma(h \rightarrow AA) = \frac{1}{32\pi} \frac{g_{hAA}^2}{m_h} \sqrt{1 - 4m_A^2/m_h^2} \quad (4.10)$$

Using the relations between the quartic couplings  $\lambda$ 's and the physical masses and Higgs mixing parameter  $m_{12}^2$ , in the alignment limit  $|\sin(\beta - \alpha)| \approx 1$ ,  $hAA$  coupling [58] takes the following form.

$$g_{hAA} \propto (\lambda_3 + \lambda_4 - \lambda_5)v \approx \frac{\sin(\beta - \alpha)y_h^\ell(m_h^2 - m_H^2) + 2m_A^2 - m_{12}^2/\sin\beta\cos\beta}{v} \quad (4.11)$$

Expressing the quantity  $y_h^\ell \sin(\beta - \alpha)$  in terms of  $g_{hAA}$  and mass parameters we get

$$y_h^\ell \sin(\beta - \alpha) = \frac{g_{hAA}v + m_{12}^2/\sin\beta\cos\beta - 2m_A^2}{m_h^2 - m_H^2} \quad (4.12)$$

We can see from Equation 4.10 that when  $m_A \lesssim \frac{m_h}{2}$ , the only way a small branching ratio for  $\text{BR}(h \rightarrow AA)$  can be achieved is when the coupling  $g_{hAA}$  is extremely small. We should also remember from our discussion of perturbativity that, in this scenario  $m_{12}^2 \approx \frac{m_H^2}{\tan^2\beta}$ , in order to ensure perturbativity of the quartic couplings. If we demand perturbativity as well as the condition,  $g_{hAA} \approx 0$ , Equation 4.12 implies  $y_h^\ell \sin(\beta - \alpha) < 0$ . In other words, wrong-sign lepton Yukawa coupling is more favored in Scenario 1, when one demands smallness of  $\text{BR}(h_{SM} \rightarrow AA)$  as well as perturbativity of the quartic couplings.

The other possibility is to consider the case when the heavier CP even scalar is the SM-like Higgs, ie  $m_H = 125$  GeV, which is our Scenario 2. However, in this case the LEP limit implies either  $m_A$  or  $m_h$  can be less than  $\frac{m_H}{2}$  [65]. We consider the low mass pseudoscalar and therefore  $m_h > \frac{m_H}{2}$ . Here the decay width of 125-GeV Higgs decaying to a pair of pseudoscalars is given by

$$\Gamma(H \rightarrow AA) = \frac{1}{32\pi} \frac{g_{HAA}^2}{m_h} \sqrt{1 - 4m_A^2/m_h^2} \quad (4.13)$$

Here too, like the previous scenario, the limit on  $\text{BR}(H \rightarrow AA)$  will indicate extremely small value of the coupling  $g_{HAA}$ , whose expression in the alignment limit ie.  $|\cos(\beta - \alpha)| \approx 1$  is given as follows:

---

<sup>1</sup>The limit is taken on the strongest side in our analysis. It may become slightly relaxed with varying  $m_A$ . Thus our study is conservative.

$$g_{HAA} \propto (\lambda_3 + \lambda_4 - \lambda_5)v \approx \frac{\cos(\beta - \alpha)y_H^\ell(m_H^2 - m_h^2) + 2m_A^2 - m_{12}^2/\sin\beta\cos\beta}{v} \quad (4.14)$$

Expressing the quantity  $y_H^\ell \cos(\beta - \alpha)$  in terms of  $g_{HAA}$  and mass parameters we get

$$y_H^\ell \cos(\beta - \alpha) = \frac{g_{HAA}v + m_{12}^2/\sin\beta\cos\beta - 2m_A^2}{m_H^2 - m_h^2} \quad (4.15)$$

We can see that, as we are concerned with low pseudoscalar mass here ( $m_A \lesssim \frac{m_H}{2}$ ), in the limit  $g_{HAA} \approx 0$ ,  $y_H^\ell \cos(\beta - \alpha)$  will be positive for the most part of our parameter space. Therefore we can conclude that the right-sign region will be favored in case of Scenario 2. We will see the implications of these in the next section.

#### • Signal strengths of the 125-GeV scalar

Important limits come from the signal strength measurements of the 125-GeV Higgs in various final states including  $\gamma\gamma$ ,  $ZZ$ ,  $WW$ ,  $b\bar{b}$  and  $\tau\tau$  final states [17, 18]. The experimental data indicate that the gauge boson and Yukawa couplings of the 125-GeV scalar are very close to their SM value. Therefore in our analysis we confine ourselves to the alignment limit ie.  $|y_{h/H}^V| \approx 1$  ( $y_h^V = \sin(\beta - \alpha)$  for Scenario 1 and  $y_H^V = \cos(\beta - \alpha)$  for Scenario 2) and  $|y_{h/H}^\ell|$  is also close to unity. This in turn implies that  $\tan\beta$  can not be very large in the RS region. However, in the WS region this condition gets slightly relaxed and  $|y_{h/H}^V|$  can deviate slightly further from unity, within the allowed range and  $\tan\beta$  can be large as long as  $|y_{h/H}^\ell|$  is close to 1. Another important constraint comes from the direct search for 125-GeV Higgs decaying into two light pseudoscalar final states, when it is kinematically allowed. The upper bound on this branching ratio translates into severe constraint on the parameter space of this model. We have discussed the effect of this constraint on our parameter space in detail in a previous subsection 4.3.

#### • Direct search for heavier (pseudo)scalars at the LHC:

Collider searches for the non-standard neutral scalar states also put constraints on the parameter space of interest. Such searches are performed at the LHC, in various SM final states. As we are particularly interested in the low pseudoscalar mass region with its enhanced coupling to leptons, the limits which are crucial for our analyses, come from the search for low pseudoscalar produced in association with a pair of  $b$  quarks and decaying into  $\tau\tau$  final state [66, 67]. Constraints from the search for low mass (pseudo)scalar produced in association with  $b\bar{b}$  and decaying into  $b\bar{b}$  [68, 69] has also been taken into account.

We have also taken into account the upper limits from CP-even non-standard scalars ( $h/H$ ) decaying to  $\tau\tau$  [52] final state. CMS has also looked for decay involving two non-standard Higgs bosons such as  $h/H \rightarrow AZ$  [70, 71],  $H \rightarrow hh$  [72–74] and  $h/H \rightarrow VV$  [75–77].

At the LHC, the charged Higgs search can be produced in several ways. When  $m_H^\pm < m_t$ , charged Higgs can be produced from the decay of top quark ( $t \rightarrow bH^\pm$ ). This decay

has been searched for in  $\tau\nu$  [78, 79] and  $c\bar{s}$  [80, 81] final state. These searches put an upper limit on  $\text{BR}(t \rightarrow bH^\pm) \times (H^\pm \rightarrow \tau\nu/c\bar{s})$ . The other important search mode at the LHC is  $(pp \rightarrow tbH^\pm)$  in the final states  $\tau\nu$  [79, 82] and  $c\bar{s}$  [83, 84] and  $t\bar{b}$  [85].

The most stringent bounds in the context of direct search for non-standard scalars come from  $pp \rightarrow h/H/A \rightarrow \tau\tau$  and  $pp \rightarrow tbH^\pm (H^\pm \rightarrow \tau\nu)$ . Although in Type-X model at large  $\tan\beta$ , the neutral non-standard scalars decay to  $\tau\tau$  with almost 100% BR and the charged Higgs decays to  $\tau\nu$  final state almost exclusively, the production cross-section is suppressed at large  $\tan\beta$  as the quark couplings scale as  $1/\tan\beta$ . This in turn puts an lower bound on  $\tan\beta$  [52].

#### 4.4 Allowed parameter space

Having listed all these constraints, our next task is to use them to constrain a type-X 2HDM, for both the scenarios 1 and 2. We take this up in the present section.

##### • Scenario 1:

This scenario corresponds to the case, where lighter CP-even scalar is the SM-like Higgs boson. One can further categorize this scenario with WS and RS regions depending on leptonic coupling of  $h$ , as discussed earlier. We scan our parameter space in the following ranges:

$$m_H \in [125, 870] \text{ GeV}, m_H^\pm \in [125, 870] \text{ GeV}, m_A \in [20, 100] \text{ GeV}, \tan\beta \in [20, 100], \\ \sin(\beta - \alpha) \in [0.99, 1], m_{12}^2 \in \left[ \frac{m_H^2}{\tan\beta} - 200, \frac{m_H^2}{\tan\beta} + 200 \right].$$

We also mention here that  $\lambda_6 = \lambda_7 = 0$ , as we only consider soft  $Z_2$  breaking terms.

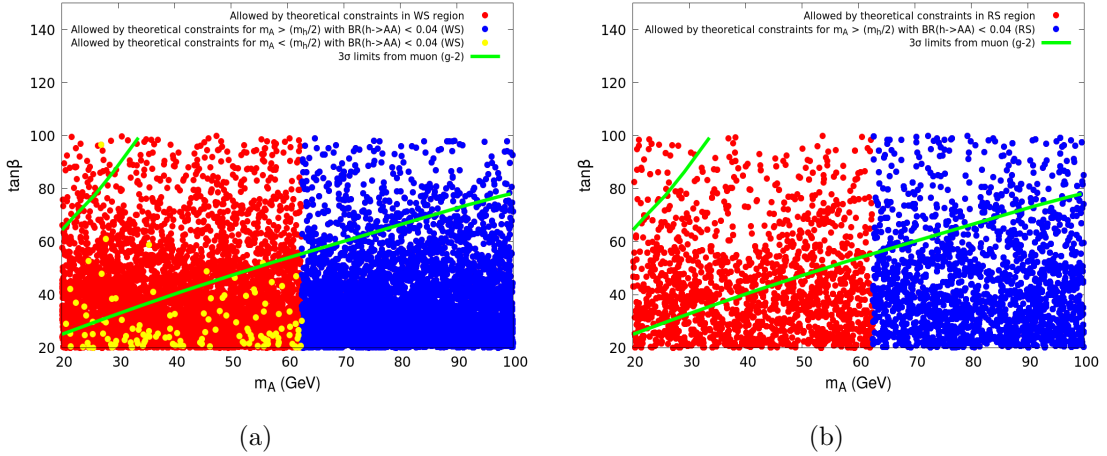


**Figure 8.** Allowed parameter spaces in  $m_A - \tan\beta$  plane for Scenario 1 with (a) WS Yukawa and (b) RS Yukawa. The green lines denote the upper and lower limits coming from the observed  $g_\mu - 2$  at  $3\sigma$  level.

In Figure 8, we see that though theoretical constraints (namely, perturbativity, unitarity and stability) prefer low to moderate  $\tan\beta$ , we can still get a large parameter space in



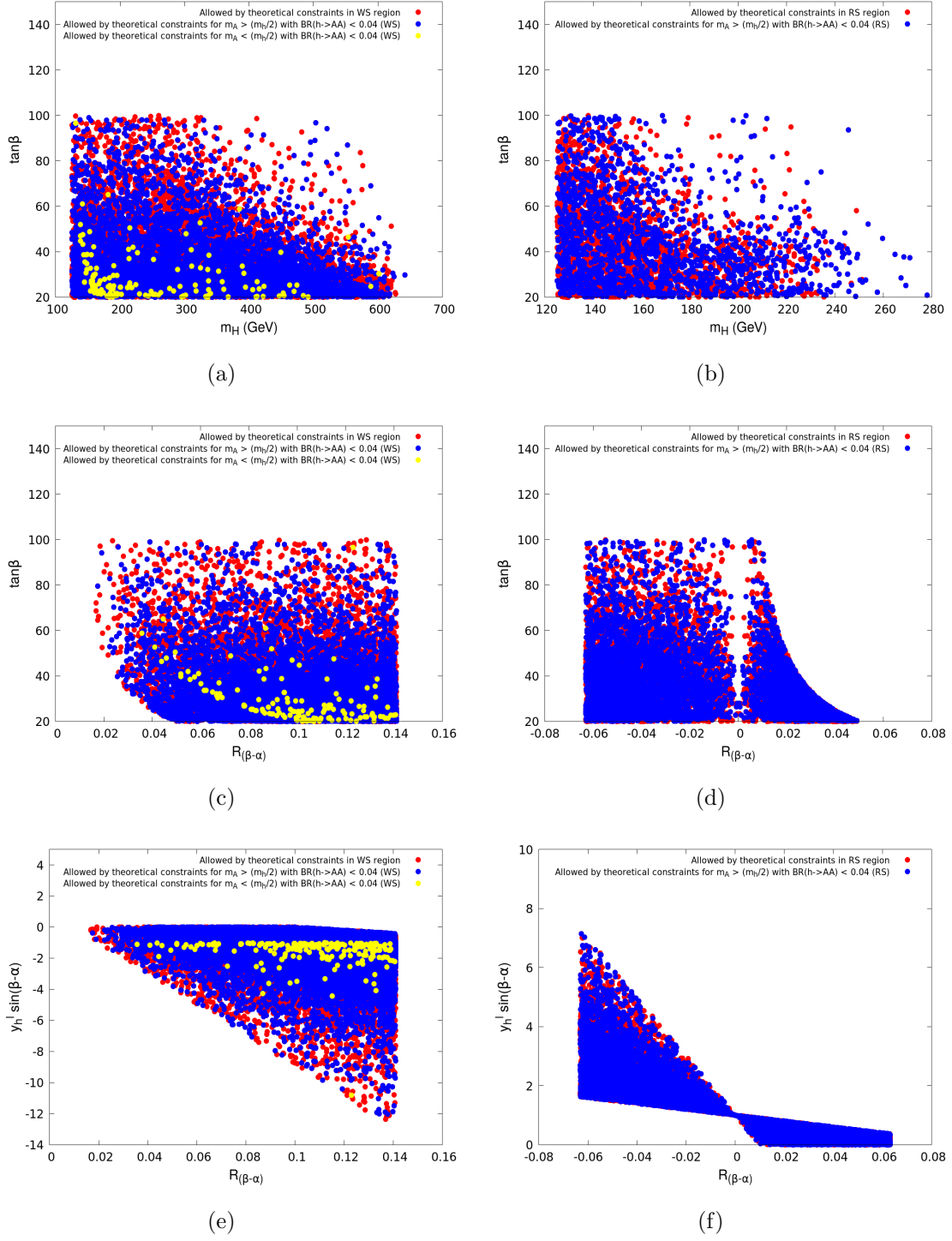


**Figure 9.** Allowed parameter spaces in scenario 1 in (a) and (b)  $m_H - \tan\beta$ , (c) and (d)  $R_{(\beta-\alpha)} - \tan\beta$ , (e) and (f)  $R_{(\beta-\alpha)} - y_h^l \times \sin(\beta-\alpha)$  plane. (a), (c) and (e) correspond to WS Yukawa, (b), (d) and (f) correspond to RS Yukawa.

WS domain which alleviates  $g_\mu - 2$  discrepancy. On the other hand, in the RS region, large  $\tan\beta$  is less favored. As discussed earlier in Section 4, we do not get a small enough  $\text{BR}(h \rightarrow AA) \lesssim 4\%$  for  $m_A \lesssim m_h/2$ , as long as we are in the RS domain. This is clear from Figure 8.

In Figure 9 (a) and (b), we show the allowed region in  $m_H - \tan\beta$  plane. We can see that moderate  $\tan\beta$  regions are favored by the theoretical constraints, especially when  $m_H$  is large. In addition to that, the upper bound from  $\text{BR}(h_{SM} \rightarrow AA)$ , pushes the allowed range of  $\tan\beta$  to further lower side.

Figure 9 (c) and (d) displays the allowed region in the  $R_{(\beta-\alpha)} - \tan\beta$  plane, where  $R_{(\beta-\alpha)}$  is defined as  $\text{sgn}[\sin(\beta - \alpha)] \times \cos(\beta - \alpha)$ . On the whole, while the RS case admits  $\sin(\beta - \alpha)$  with both signs, it is restricted to positive values only for WS. Furthermore, the WS picture disfavors large  $\tan\beta$  from the limit on  $\text{BR}(h_{SM} \rightarrow AA)$  so long as  $m_A \lesssim \frac{m_h}{2}$ .

In Figure 9 (e) and (f), we plot  $y_h^\ell \times \sin(\beta - \alpha)$  against  $R_{(\beta-\alpha)}$ . The limit on  $\text{BR}(h \rightarrow AA)$  for  $m_A \lesssim m_h/2$  does not allow much deviation of  $y_h^\ell \times \sin(\beta - \alpha)$  from unity, which is also consistent with the alignment limit. In Figure 9(f), one can see that, both positive and negative signs for  $\sin(\beta - \alpha)$  are equally consistent with the alignment limit ( $|y_h^\ell| \times \sin(\beta - \alpha) \approx 1$ ) in the RS region.

• **Scenario 2:**

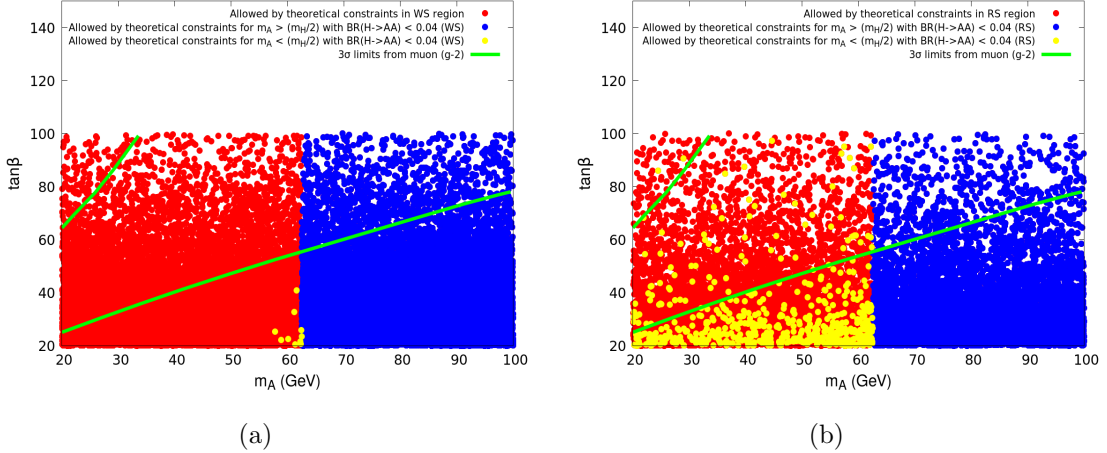


**Figure 10.** Allowed parameter spaces in  $m_A - \tan\beta$  plane for Scenario 2 with (a) WS Yukawa and (b) RS Yukawa. The green lines denote the upper and lower limits coming from the observed  $g_\mu - 2$ .

In this scenario, the heavier CP-even scalar  $H$  is the SM-like Higgs. To get the allowed regions in this scenario, we scan our parameter space in the following range:

$$m_h \in [80, 125] \text{ GeV}, m_H^\pm \in [80, 180] \text{ GeV}, m_A \in [20, 100] \text{ GeV}, \tan\beta \in [20, 100], \\ \cos(\beta - \alpha) \in [0.99, 1], m_{12}^2 \in \left[ \frac{m_H^2}{\tan\beta} - 200, \frac{m_H^2}{\tan\beta} + 200 \right].$$

In Figures 10 and 11, we plot the points allowed by theoretical constraints as well as constraints on  $\text{BR}(H \rightarrow AA)$ , in two-dimensional planes of various model parameters.

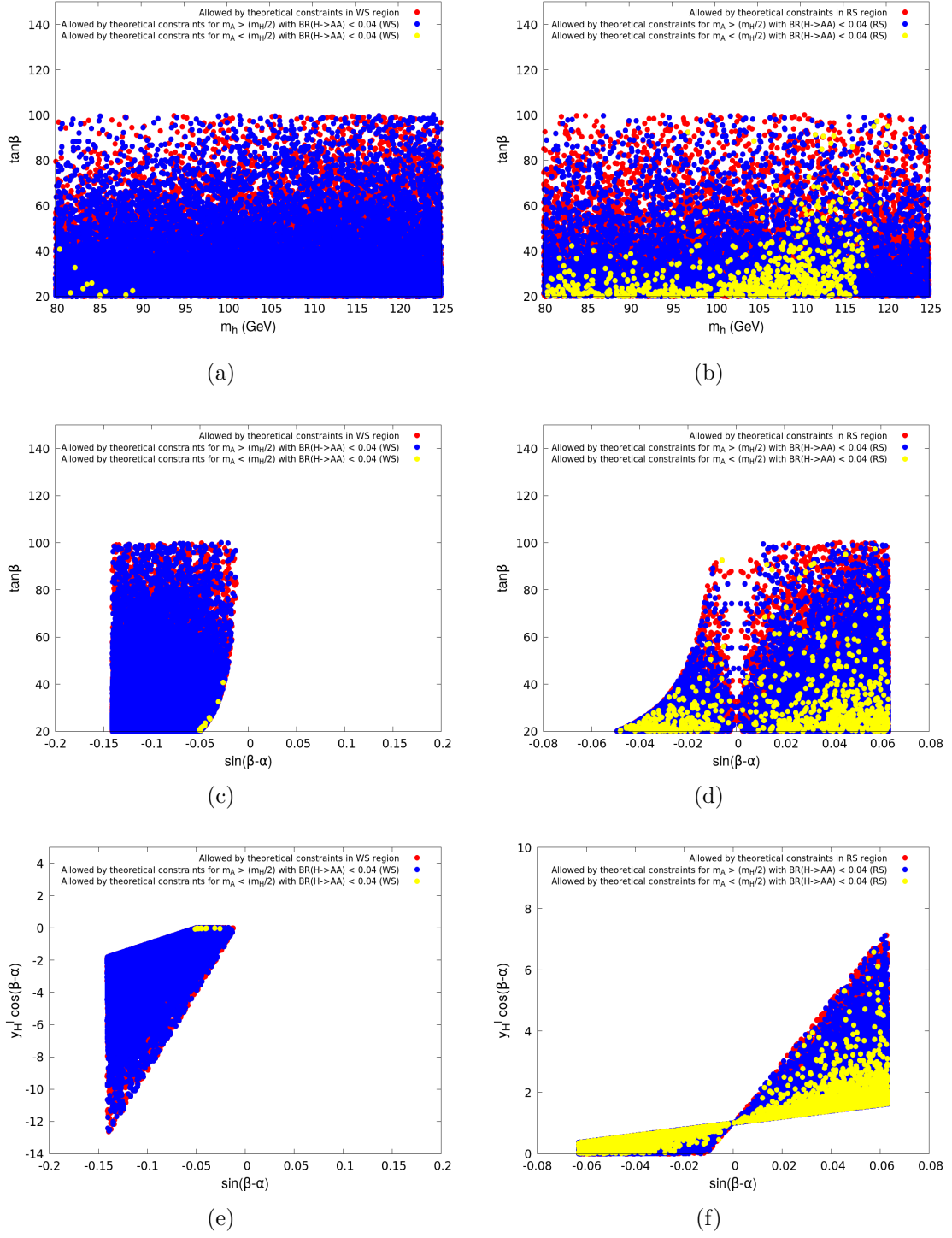


**Figure 11.** Allowed parameter spaces in scenario 2 in (a) and (b)  $m_H - \tan\beta$ , (c) and (d)  $\sin(\beta - \alpha) - \tan\beta$ , (e) and (f)  $\sin(\beta - \alpha) - y_H^l \times \sin(\beta - \alpha)$  plane. (a),(c) and (e) correspond to WS Yukawa, (b),(d) and (f) correspond to RS Yukawa.

If we focus on Figure 10(a), it becomes clear that for  $m_A \lesssim \frac{m_H}{2}$ , the constraints on  $HAA$  coupling can leave a very narrow region near resonance  $m_A \approx m_H/2$ , for WS cases, which is not quite compatible with the  $g_\mu - 2$  observation, within  $3\sigma$ . But the situation will be more relaxed in the RS domain for scenario 2 (yellow points in Figure 10(b)). On the other hand, we can get a large parameter space both in WS and RS region, which can solve  $g_\mu - 2$  discrepancy, for  $m_A > \frac{m_H}{2}$ .

In Figure 11 (a) and (b), the allowed regions in  $m_h - \tan \beta$  plane are shown for the WS and RS respectively. We can see that, in the RS case, low to moderate  $\tan \beta$  will be favored from the requirement of low  $\text{BR}(h_{SM} \rightarrow AA)$ . However, when the difference between the lighter and heavier CP-even scalar masses decreases, even larger  $\tan \beta$  becomes allowed.

In Figure 11 (c) and (d), we show the allowed region in  $\sin(\beta - \alpha) - \tan \beta$  plane where both positive and negative  $\sin(\beta - \alpha)$  is allowed for RS cases, but WS is attained with only negative  $\sin(\beta - \alpha)$ .

In Figure 11 (e) and (f), one can see similar behavior as scenario 1, where small  $\text{BR}(H \rightarrow AA)$  for  $m_A \lesssim \frac{m_H}{2}$  prefers lepton Yukawa coupling  $y_h^\ell$  close to unity, consistent with the observed Higgs signals for both WS and RS cases.

## 5 The running of various couplings

### 5.1 The Renormalization Group Equations(RGEs)

The parameters constrained above are considered at the electroweak scale, set at the pole mass of top quark ( $\sim 173.34$  GeV). We now investigate how they evolve at higher scales and thus obtain their domain of validity in the light of vacuum stability(following [57]) and perturbative unitarity(following [55]). This yields the cut-off scale  $\Lambda_{UV}^{cut-off}$ .

In this subsection we present the one-loop RG equations for the various quartic couplings as well as the gauge and third generation Yukawa couplings. For actual presentation of our results, we will take recourse to the two-loop renormalization group equations [86] for enhanced precision and rigor. However, we will soon see that, qualitatively the evolution trajectories at the one- and two-loop levels are very similar in our case and that the quantitative differences are rather minor, at least at energy scales well below the perturbative limits of couplings. Keeping this in view, we start by presenting the one-loop RGEs so that we can fall back on them to provide intuitive explanations of the trajectories. At the same time, the detailed results presented in the next subsection are all based on two-loop equations, although we take the liberty of explaining them in terms of one-loop equations, empowered by reasons summarized above.

First we present the one-loop RGEs for the gauge couplings. They form a stand-alone set, at one loop, as we can see from Equation 5.1, and therefore they remain unchanged for different types of 2HDMs. We mention here that in writing Equation 5.1, GUT normalization has not been used.

$$\begin{aligned}
16\pi^2\beta_{g_1} &= 7g_1^3 \\
16\pi^2\beta_{g_2} &= -3g_2^3 \\
16\pi^2\beta_{g_3} &= -7g_3^3
\end{aligned} \tag{5.1}$$

Next we focus on the RGE of the Yukawa couplings in Type-X 2HDM. The corresponding equations are as follows. Here  $g$  and  $Y$  in the superscripts, respectively, denote gauge and Yukawa interactions, contributing to the running of the Yukawa couplings (taken here as real).

$$\begin{aligned}
16\pi^2\beta_{Y_t}^g &= -\left(\frac{17}{12}g_1^2 + \frac{9}{4}g_2^2 + 8g_3^2\right)Y_t \\
16\pi^2\beta_{Y_t}^Y &= \left(\frac{3}{2}Y_b^2 + \frac{9}{2}Y_t^2\right)Y_t \\
16\pi^2\beta_{Y_b}^g &= -\left(\frac{5}{12}g_1^2 + \frac{9}{4}g_2^2 + 8g_3^2\right)Y_b \\
16\pi^2\beta_{Y_b}^Y &= \left(\frac{9}{2}Y_b^2 + \frac{3}{2}Y_t^2\right)Y_b \\
16\pi^2\beta_{Y_\tau}^g &= -\left(\frac{15}{4}g_1^2 + \frac{9}{4}g_2^2\right)Y_\tau \\
16\pi^2\beta_{Y_\tau}^Y &= \frac{5}{2}Y_\tau^3
\end{aligned} \tag{5.2}$$

The resulting beta-function will be the sum of the gauge and Yukawa components.

$$\beta_Y = \beta_Y^g + \beta_Y^Y \tag{5.3}$$

The Yukawa and gauge contributions show similar behavior for  $Y_t$  and  $Y_b$ . It is clear from Equations. 5.2 that the gauge contribution decreases with energy whereas the Yukawa part go up at higher energy. However, the terms involving the strong coupling constant  $g_3$  dominates over the other terms and therefore the top and bottom Yukawa couplings monotonically decrease with energy. The  $\tau$ -Yukawa coupling on the other hand, unaffected by the strong interaction, remains almost constant. This behavior can be seen from Figure 15.

The relevant equations for the running of quartic couplings are given below. Here, the superscripts  $b$  and  $Y$  denote, respectively, bosonic (gauge couplings and quartic couplings) and Yukawa interactions, contributing to the running of  $\lambda$ 's.

$$\begin{aligned}
16\pi^2\beta_{\lambda_1}^b &= \frac{3}{4}g_1^4 + \frac{3}{2}g_1^2g_2^2 + \frac{9}{4}g_2^4 - 3g_1^2\lambda_1 - 9g_2^2\lambda_1 + 12\lambda_1^2 + 4\lambda_3^2 + 4\lambda_3\lambda_4 + 2\lambda_4^2 + 2\lambda_5^2 \\
16\pi^2\beta_{\lambda_1}^Y &= -4Y_\tau^4 + 4Y_\tau^2\lambda_1 \\
16\pi^2\beta_{\lambda_2}^b &= \frac{3}{4}g_1^4 + \frac{3}{2}g_1^2g_2^2 + \frac{9}{4}g_2^4 - 3g_1^2\lambda_2 - 9g_2^2\lambda_2 + 12\lambda_2^2 + 4\lambda_3^2 + 4\lambda_3\lambda_4 + 2\lambda_4^2 + 2\lambda_5^2 \\
16\pi^2\beta_{\lambda_2}^Y &= -12Y_b^4 - 12Y_t^4 + (12Y_b^2 + 12Y_t^2)\lambda_2
\end{aligned}$$

$$\begin{aligned}
16\pi^2\beta_{\lambda_3}^b &= \frac{3}{4}g_1^4 - \frac{3}{2}g_1^2g_2^2 + \frac{9}{4}g_2^4 - 3g_1^2\lambda_3 - 9g_2^2\lambda_3 \\
&\quad + (\lambda_1 + \lambda_2)(6\lambda_3 + 2\lambda_4) + 4\lambda_3^2 + 2\lambda_4^2 + 2\lambda_5^2 \\
16\pi^2\beta_{\lambda_3}^Y &= (6Y_b^2 + 6Y_t^2 + 2Y_\tau^2)\lambda_3 \\
16\pi^2\beta_{\lambda_4}^b &= 3g_1^2g_2^2 - (3g_1^2 + 9g_2^2)\lambda_4 + 2\lambda_1\lambda_4 + 2\lambda_2\lambda_4 + 8\lambda_3\lambda_4 + 4\lambda_4^2 + 8\lambda_5^2 \\
16\pi^2\beta_{\lambda_4}^Y &= (6Y_b^2 + 6Y_t^2 + 2Y_\tau^2)\lambda_4 \\
16\pi^2\beta_{\lambda_5}^b &= (-3g_1^2 - 9g_2^2 + 2\lambda_1 + 2\lambda_2 + 8\lambda_3 + 12\lambda_4)\lambda_5 \\
16\pi^2\beta_{\lambda_5}^Y &= (6Y_b^2 + 6Y_t^2 + 2Y_\tau^2)\lambda_5
\end{aligned} \tag{5.4}$$

Like before, the actual beta-function will be the sum of the bosonic and Yukawa components.

$$\beta_\lambda = \beta_\lambda^b + \beta_\lambda^Y \tag{5.5}$$

One should note, since the Yukawa couplings depend on the specific kinds of 2HDM, it is obvious that their evolution as well as those of the quartic couplings are model-dependent. This is obvious from Equations. 5.2 and 5.4.

## 5.2 Coupling trajectories and inference drawn from them

In this subsection, the running of various couplings will be illustrated in terms of a few chosen benchmark points. A brief justification for choosing those will be given shortly. Based on the discussion in the preceding subsection, we will present here the full two-loop results for our benchmark points(BP). Our chosen benchmarks are consistent with theoretical as well as experimental constraints.

We have seen that, in Scenario 1, the requirement of low branching fraction of SM-like Higgs to two pseudoscalars along with other constraints leads us to  $m_A > \frac{m_h}{2}$  in the RS region. However, it is possible to get allowed points in the whole range of  $m_A$  in the WS regime. Keeping this in mind, we choose three benchmarks BP1, BP2 and BP3 for scenario 1. BP1 corresponds to WS region with  $m_A > \frac{m_h}{2}$ . BP2 corresponds to WS region and  $m_A < \frac{m_h}{2}$ . For BP3, we have taken RS with  $m_A > \frac{m_h}{2}$ . We present the benchmark points chosen for Scenario 1 in Table 1.

As long as we are in the alignment limit with large  $\tan\beta$ ,  $\lambda_2$  is precisely determined by SM-like Higgs with a very small value( $\approx \frac{m_h^2}{v^2} \approx 0.258$ ), which is the case for all the benchmarks in Table 1. On the other hand,  $\lambda_1$  and  $\lambda_3$  depend on the the mass splitting between two CP-even scalars. Furthermore,  $\lambda_1$  can be controlled by  $m_{12}^2$ , which gets an enhancement factor in the large  $\tan\beta$  region. As for this parameter space, we have  $m_{12}^2 \sim \frac{m_H^2}{\tan\beta}$  with large  $\tan\beta$ ,  $\lambda_4$  is proportional to  $m_A^2 - 2m_{H^\pm}^2 + m_H^2$  and takes a negative value for our benchmarks. Similarly,  $\lambda_5$  takes a value close to  $\lambda_4$  with a opposite sign, being proportional to  $-m_A^2 + m_H^2$ . It is clearly seen that for degenerate  $m_H$  and  $m_{H^\pm}$ ,  $\lambda_5 \approx -\lambda_4$ . The equality in magnitude is prominent in case of large  $m_H$ . For BP3 this does not apply. However, the mutual opposite sign between  $\lambda_4$  and  $\lambda_5$  still holds. We would

	BP1	BP2	BP3
$m_H$ in GeV	449.734	324.237	153.865
$m_A$ in GeV	80.0	24.6997	63.0
$m_{H^\pm}$ in GeV	453.895	331.34	176.152
$\lambda_1$	0.095392	1.4963	0.52616
$\lambda_2$	0.25788	0.25792	0.25773
$\lambda_3$	6.9130	3.5968	0.52559
$\lambda_4$	-3.3549	-1.8783	-0.56774
$\lambda_5$	3.23062	1.72343	0.324993
$m_{12}^2$ in $GeV^2$	2696.2389	1992.85	353.226215
$\tan \beta$	75.0	52.7154	67.0
$\sin(\beta - \alpha)$	0.9996	0.999163	0.999996
$y_h^\ell \times \sin(\beta - \alpha)$	-1.12095144	-1.15624366	0.81048833

**Table 1.** *Benchmark points for Scenario 1.*

like to mention here that all the benchmarks satisfy the limit on  $y_h^\ell$  as well as  $y_h^V$  from the alignment condition [17, 18].

In Figure 12, we can see the two-loop RG running of quartic couplings for BP1, BP2 and BP3. For all these benchmarks tree level unitarity decides the value of  $\Lambda_{UV}^{cut-off}$  which is denoted by the end scale in all figures, whereas stability and perturbativity can be satisfied even after that cut-off scale. It is clear from the running that the larger the value for any quatic coupling at the electroweak scale, the quicker it breaks the unitarity criteria. For both BP1 and BP2,  $\lambda_3$  is becomes largest among the quartic couplings at the breakdown scale, whereas in BP3  $\lambda_1$  plays this role. Also from Figure 12(c) it is clear that starting from nearly same value,  $\lambda_1$  can increase faster than  $\lambda_3$  as energy increases. On the other hand, the runnings of other  $\lambda$ 's show a flat nature compared to  $\lambda_1$  and  $\lambda_3$ . As we do not allow hard  $Z_2$ -breaking,  $\lambda_6$  and  $\lambda_7$  do not change with energy and are fixed at zero. In explicit terms, the RG equations for  $\lambda_6$  and  $\lambda_7$ , always carry the terms proportional to these two  $\lambda$ 's and therefore the relation  $\frac{d\lambda}{d\mu} = 0$  remains valid throughout the running .

A complementary picture is noticed in Scenario 2. Here the requirement of low branching fraction of SM-like Higgs to a pair of pseudoscalars along with other constraints pushes  $m_A > \frac{m_H}{2}$  in the WS region. On the other hand, in the RS case, it is possible to get a low  $BR(h_{SM} \rightarrow AA)$  in the entire range of  $m_A$ . To examine Scenario 2 on a case by case basis, we choose three benchmarks BP4, BP5, BP6. BP4 corresponds to RS region with  $m_A > \frac{m_H}{2}$ , BP5 corresponds to RS region with  $m_A < \frac{m_H}{2}$ . We consider WS region with  $m_A > \frac{m_H}{2}$  in BP6. The benchmarks for Scenario 2 are listed in Table 2. We mention here that although it is possible to get a few points in the WS region, with  $m_A \lesssim \frac{m_H}{2}$ , in the resonant region with severe fine-tuning, we do not consider this region further in our analysis.

Our BP4 and BP6 have negative  $\sin(\beta - \alpha)$  and large  $\tan \beta$ , where BP5 has positive  $\sin(\beta - \alpha)$  and comparatively small  $\tan \beta$ . Here too, in the alignment limit,  $\lambda_2$  is governed by the 125-GeV Higgs mass and therefore for all the benchmarks it gets similar values as

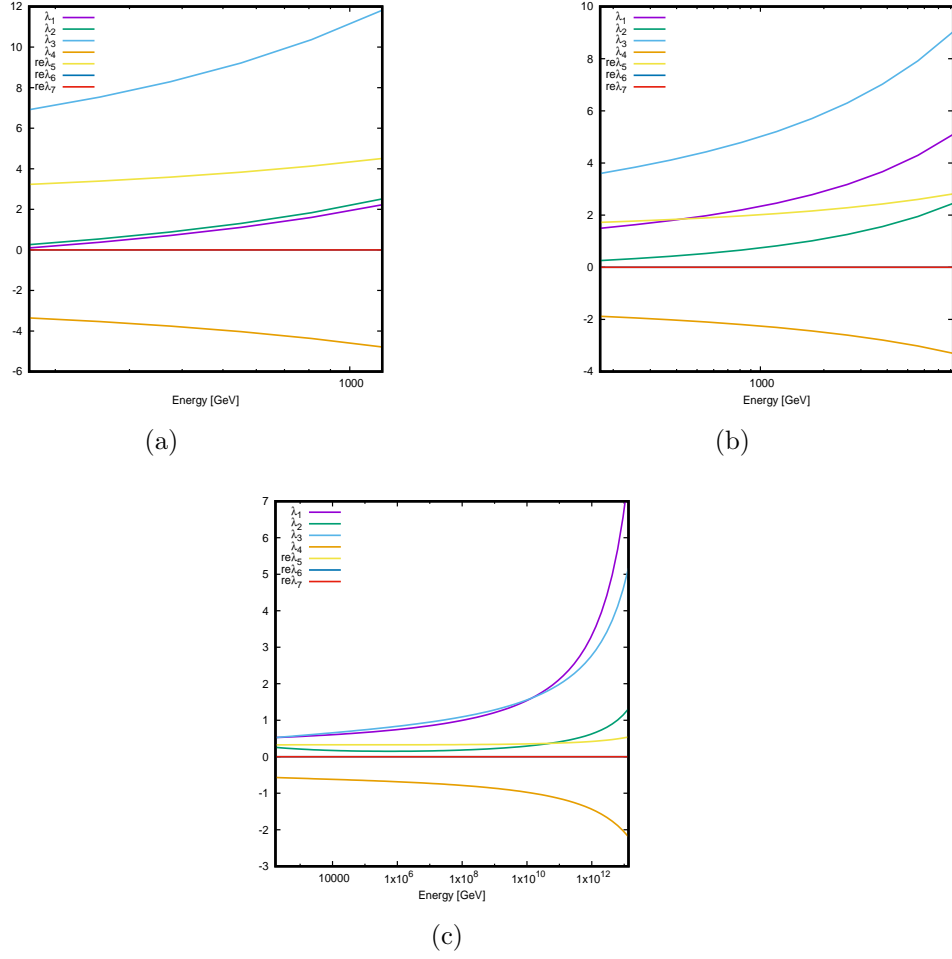


**Figure 12.** Two-loop RG running of quartic couplings for the benchmarks (a) BP1, (b) BP2 and (c) BP3 from Scenario 1.

	BP4	BP5	BP6
$m_H$ in GeV	117.409	93.6073	121.448
$m_A$ in GeV	70.0	15.7859	63.0
$m_{H^\pm}$ in GeV	142.529	135.00	139.871
$\lambda_1$	0.07121	1.0251	0.082024
$\lambda_2$	0.25774	0.25767	0.25774
$\lambda_3$	0.46960	0.58636	0.38712
$\lambda_4$	-0.3372	-0.45412	-0.33662
$\lambda_5$	0.121841	0.138905	0.177861
$m_{12}^2$ in $GeV^2$	168.10299	393.28757	204.844987
$\tan \beta$	82.0	22.0	72.00
$\sin(\beta - \alpha)$	-0.00141421	0.00601127	-0.02828
$y_h^\ell \times \cos(\beta - \alpha)$	0.88403289597	1.13220955	-1.036145

**Table 2.** Benchmark points for Scenario 2.



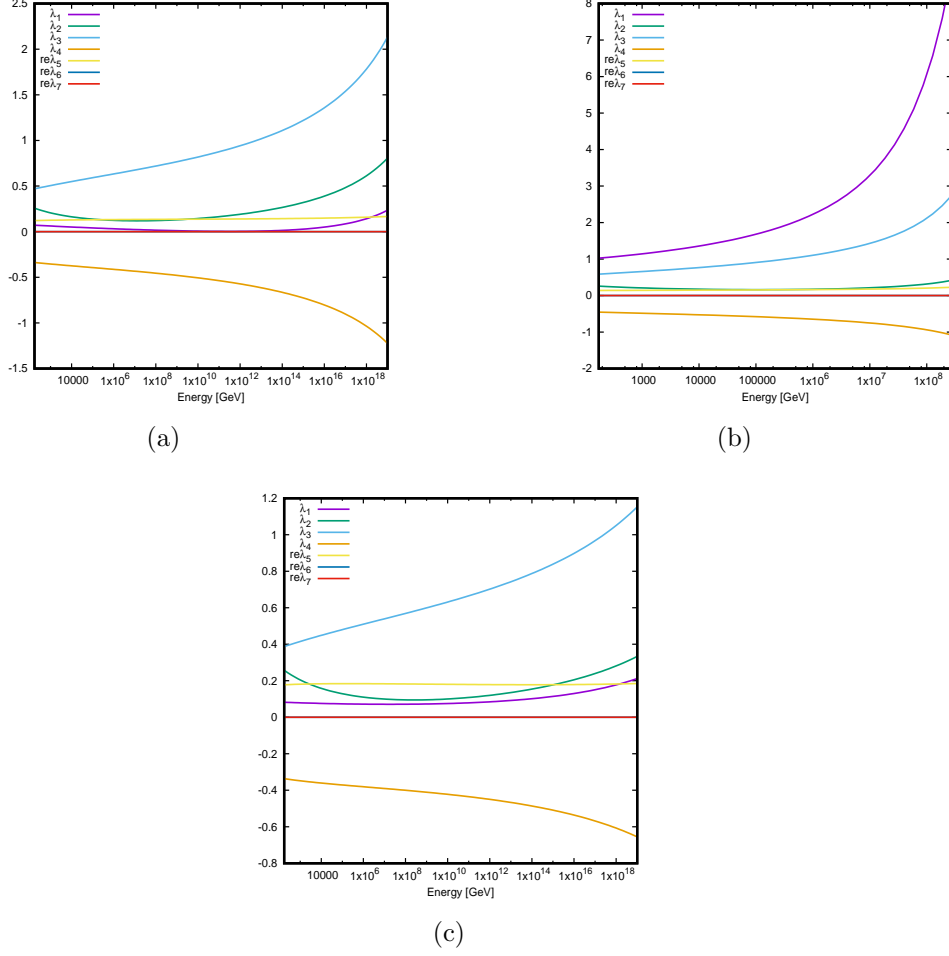


**Figure 13.** Two-loop RG running of quartic couplings for the benchmarks (a) BP4, (b) BP5 and (c) BP6 from Scenario 2 .

scenario 1. In this case,  $\lambda_3$  is comparatively smaller than the previous case due to smaller mass gap between  $m_H$  and  $m_h$ , whereas  $\lambda_1$  can get somewhat enhanced contribution from  $m_{12}^2$  term at large  $\tan\beta$ . On the other hand,  $\lambda_4$  and  $\lambda_5$  are opposite in sign, similar to the previous scenario.

Having thus identified our benchmark points, we further note that all the six aforesaid benchmark points fall in the yellowish interior region of Figure 5. Therefore our analyses based on them are legitimate, both with the older data and on taking the very recent results into account, as far as constraints from  $g_\mu - 2$  is concerned. For our subsequent analysis on UV-completion, we shall use the combined data of  $g_\mu - 2$  as the constraining factor on the parameter space.

In Figure 13, we display two-loop RG running of quartic couplings for BP4, BP5 and BP6. We can see that for all the three benchmarks  $\Lambda_{UV}^{cut-off}$  is again decided by tree level unitarity. For BP4 and BP6, comparatively smaller values of  $\lambda$ 's at the electroweak scale ensure tree-level unitarity as well as perturbativity and stability upto very high scale ( $\sim 10^{19}$  GeV). We can see that in general it is easier to achieve UV-completion for scenario 2 than 1.

We have noticed in Figures 12 and 13 that for all the  $\lambda$ 's, the negative contribution to the running of  $\lambda$ 's comes from the combination  $(3g_1^2 + 9g_2^2)\lambda$  and terms involving Yukawa couplings. If to this we couple the information that  $g_2$  falls at higher energies, while  $g_1$  has at best marginal rise and the Yukawa couplings remain more or less constant, one finally has all quartic couplings rising with energy in this scenario. This feature which is generic to 2HDMs is due to the proliferation of bosonic degrees of freedom in the RG equations. Thus the stronger constraint almost invariably comes from perturbative unitarity.

The quartic coupling  $\lambda_2$  shows a unique behavior. For some benchmarks (namely BP1 and BP2) it shows the usual monotonically increasing trend. But for the other BPs (BP3 to BP6) it decreases initially and then increases. The reason behind this behavior is the following: in case of BP1 and BP2 the magnitude of  $\lambda_3, \lambda_4$  and  $\lambda_5$  are much larger compared to the rest of the benchmarks. The terms proportional to  $\lambda_3, \lambda_4$  and  $\lambda_5$  control the positive contribution to the beta function for  $\lambda_2$ . Therefore depending on their values the cancellation between the positive and negative terms can sometimes, take place. However, here the dominant negative contribution comes from terms involving Yukawa couplings and their strengths drop at higher energies. Thus  $\lambda_2$  starts to increase at high energies for all the benchmarks. One can also note that this behavior is correlated to the mass difference between the two neutral scalars  $h$  and  $H$  as the coupling  $\lambda_3$  is proportional to this mass difference. It is evident from Table 1 that in case of BP1 and BP2, this mass difference is much larger. Consequently, the beta function for  $\lambda_2$  takes a positive value in these cases at all energies.

On the other hand, in case of BP3, we see that  $\lambda_1$  and  $\lambda_3$  start from similar low energy values, but  $\lambda_1$  tends to grow faster. As in this case  $\lambda_1, \lambda_3 > \lambda_2, \lambda_4$ , the bosonic contribution is larger in case of  $\lambda_1$  compared to  $\lambda_3$ . The Yukawa contributions drop with energy whereas the bosonic contribution keeps growing. Therefore, beyond a certain energy ( $\sim 10^{10}$  GeV),  $\lambda_1$  becomes larger than  $\lambda_3$ .

Another interesting feature can be observed if we compare the running of  $\lambda_4$  and  $\lambda_5$  in case of BP1 and BP2. In these two cases, at the EW scale,  $|\lambda_4| \approx |\lambda_5|$  as can be seen from Table 1. It can be checked from Equation 5.4 that in this limit, the beta functions for  $\lambda_4$  and  $\lambda_5$  become almost equal to each other in magnitude and opposite in sign. This behavior is clearly seen in Figure 12.

A comparison has been made between one-loop and two-loop RG running of quartic couplings in Figure 14, for a representative benchmark (BP3). We have seen that in case of one-loop RG evolution unitarity breaks down faster than the two-loop case. However, the breaking scale is of the order of  $10^{13}$  GeV in both cases. The values of quartic couplings, too, are very similar at high scales. Nonetheless, it is seen that the two-loop contribution helps us achieve somewhat higher UV cut-off scales.

The running of the gauge and Yukawa couplings are shown in case of BP3 and BP4 in Figure 15. The qualitative nature of the running will be same for all the benchmarks. The variation in the top- and bottom-Yukawa couplings are significant, as can be seen through the logarithmic plots, since they are affected by strong interaction, unlike what happens to the  $\tau$ -Yukawa. The  $\tau$ -Yukawa interaction overrides even the top-Yukawa coupling at high

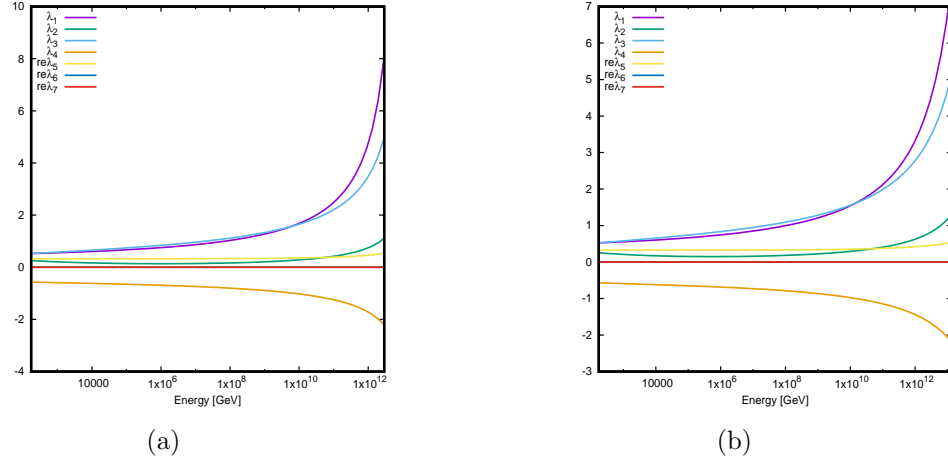


**Figure 14.** (a) One-loop and (b) two-loop RG running of quartic couplings for BP3.

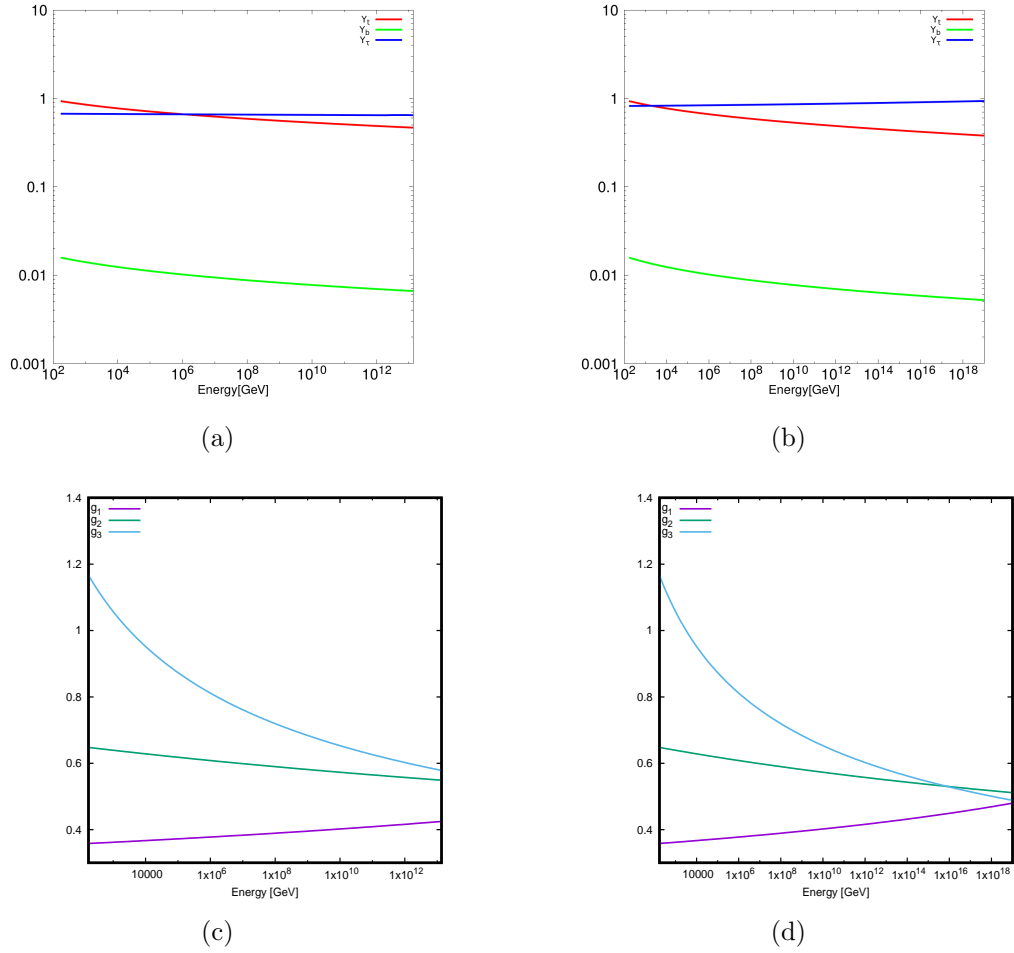


**Figure 15.** Two-loop RG running of third generation Yukawa couplings for (a) BP3 and (b) BP4 and gauge couplings for (c) BP3 and (d) BP4 respectively.

scales, by virtue of the fact that we are considering benchmark points with large  $\tan\beta$ .

Some remarks are in order on the evolution of the gauge couplings, especially in the context of possible embedding of the Type-X 2HDM in a Grand Unified Theory (GUT). As far as the gauge interactions are concerned, the evolution patterns are largely similar to the SM trajectories, if one remembers that GUT normalization has not been used for the  $U(1)$  gauge coupling. It should also be noted that one loses perturbative unitarity of quartic couplings at around  $10^{13}$  GeV for BP3, and even the two-loop RGEs cease to be trustworthy beyond that. So long as perturbativity is held to be sacrosanct, one therefore needs the intervention of new physics within approximately  $10^{13}$  GeV in this case, and that intervening physics should have a role in ensuring grand unification, if at all. For BP4, on the other hand, no such requirement arises since the interactions are perturbative all the way to the Planck scale. However, the merger of the three kinds of gauge interaction at the GUT scale still requires some additional threshold effects, as much as they do in the standard model, a requirement eminently fulfilled, for example, by supersymmetry broken at the TeV-scale.

## 6 Allowed regions with various cut-off scales

After discussing the RG-evolutions of all the relevant couplings in the model, we proceed to scan the model parameter space and look for points which satisfy all the theoretical constraints, namely perturbativity, unitarity and vacuum stability upto cut-off scale  $\Lambda_{UV}^{cut-off} (\sim 10^4, 10^8, 10^{16}, 10^{19} \text{ GeV})$ . To maintain consistency in the discussion we divide our analysis in four previously considered scenarios namely,

- 1) Case 1: Scenario 1 with WS Yukawa,
- 2) Case 2: Scenario 1 with RS Yukawa,
- 3) Case 3: Scenario 2 with WS Yukawa,
- 4) Case 4: Scenario 2 with RS Yukawa.

We will identify the allowed parameter spaces for each of these cases in two-dimensional planes of relevant physical model parameters as well as the quartic couplings  $\lambda$ 's. In all the plots in Figure 16-27 the blue, green, red and yellow points represent the regions valid upto  $10^4, 10^8, 10^{16}, 10^{19}$  GeV respectively.

### • Case 1:

In Figure 16(a), the two black lines represent the upper and lower bounds from  $g_\mu - 2$  anomaly at  $3\sigma$ . Figure 16(b) shows the allowed parameter space which satisfy the observed  $g_\mu - 2$  as well as the strong upper limit from  $\text{Br}(h_{SM} \rightarrow AA)$ . It is clear from this plot that high-scale validity upto the Planck scale demands  $\tan\beta \lesssim 30$ . At the electroweak scale we have seen that large  $\tan\beta$  regions are disfavored from the requirement of perturbative unitarity, since large  $\tan\beta$  eventually results in large  $\lambda$ 's. For high-scale validity,  $\lambda$ 's need to be small at electroweak scale. Naturally, relatively small values of  $\tan\beta$  are favored from the stand-point of high-scale validity. On the other hand, the observed  $g_\mu - 2$  prefers

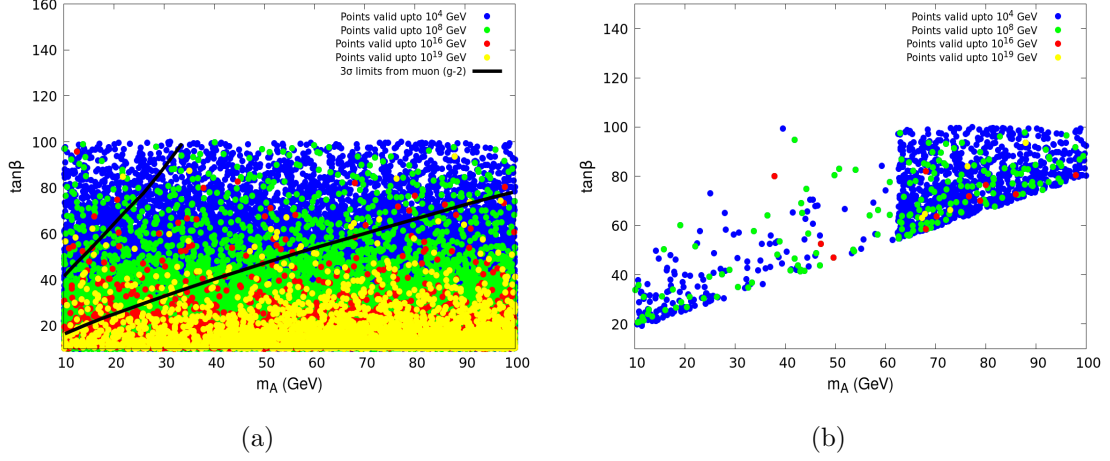


**Figure 16.**  $m_A - \tan\beta$  plane, valid upto different energy scales after applying (a) theoretical constraints (b) theoretical constraints +  $(g_\mu - 2)$  at  $3\sigma$  +  $BR(h_{SM} \rightarrow AA)$  bounds for Case 1.

$\tan\beta$  on the higher side, rendering a very tiny region valid upto the Planck scale, which is clear from Figure 16(b). In the same figure, we see a sharp discontinuity in the allowed parameter space around  $m_A \approx m_h/2$ . This is because of the fact that when  $m_A \lesssim \frac{m_h}{2}$ , one is strongly restricted by the limit  $BR(h_{SM} \rightarrow AA) \lesssim 4\%$ . This constraint is particularly severe for large  $\tan\beta$ , a feature we have already seen in Section 4.

In Figures 17(a), (b) and (c), we show the high-scale validity in the  $(m_H - \tan\beta)$ ,  $(\sin(\beta - \alpha) - \tan\beta)$  and  $(m_H - m_{H^\pm})$  planes respectively. We can see that the high-scale validity demands smaller  $m_H$ . The major reason behind this is the following. As  $\lambda_3$  increases with  $m_H$  in this region (see Equation 4.3), the requirement of small  $\lambda_3$  at the electroweak scale (which is necessary for high-scale validity) pushes us towards small  $m_H$  values. One more feature from the figure is that, when  $\tan\beta \lesssim 50$  there is a discontinuity in the allowed points. The reason behind this is the following. The parameter space with  $\tan\beta \lesssim 50$  and  $m_A > \frac{m_h}{2}$ , albeit allowed by the  $BR(h_{SM} \rightarrow AA)$  constraints, faces severe constraint from the lower limit on  $(g_\mu - 2)$  (see Figure 16(a)). On the other hand, the small strip below  $\tan\beta \lesssim 50$  corresponds to the points where  $m_A \lesssim \frac{m_h}{2}$  and  $BR(h_{SM} \rightarrow AA)$  upper limit is satisfied. Similar feature is observed in Figure 17(b) where the small strip below  $\tan\beta \lesssim 50$  corresponds to  $m_A \lesssim \frac{m_h}{2}$ . From Figure 17(c), we can see that the high-scale validity puts a strong upper bound on  $m_H$ , which also follows from our understanding of the perturbativity and unitarity condition at the electroweak scale. The degeneracy between  $m_H$  and  $m_{H^\pm}$  mass naturally pushes the charged scalar mass to smaller values, at the high scales which is evident from the Figure 17(c).

Let us now discuss the high-scale validity in the planes spanned by the quartic couplings, as they play the key role in this regard. In Figure 18(a), we can see that  $\lambda_1$  controls the high-scale behavior much more than  $\lambda_2$ . This happens because  $\lambda_2$  at the electroweak scale is solely determined by the 125-GeV Higgs mass and varies only slightly with energy, a behavior we have already seen. With the variation in scale from  $10^4$  GeV to  $10^{19}$  GeV,

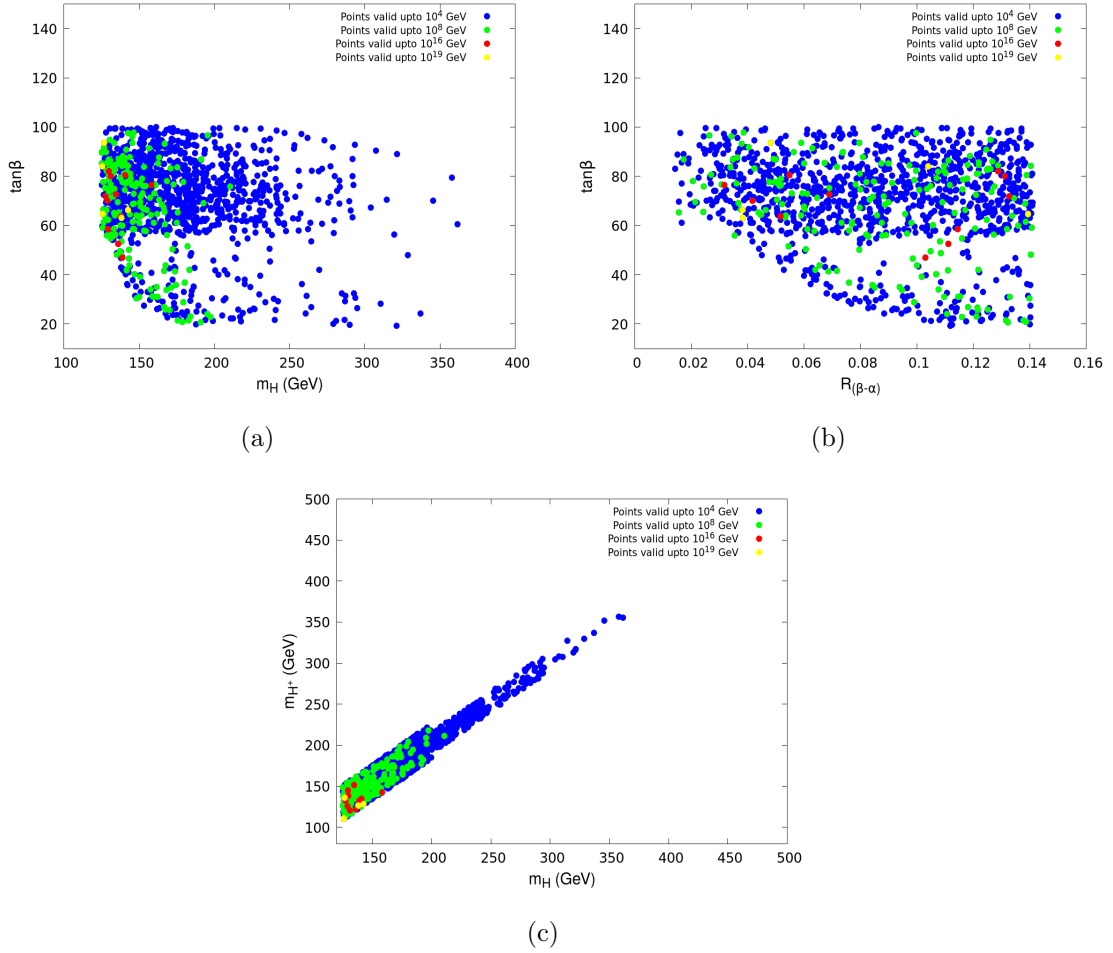


**Figure 17.** (a)  $m_H - \tan\beta$ , (b)  $R_{(\beta-\alpha)} - \tan\beta$  and (c)  $m_H - m_{H^\pm}$  plane, valid upto different energy scales after applying theoretical constraints +  $(g_\mu - 2)$  at  $3\sigma$  +  $BR(h_{SM} \rightarrow AA)$  bounds for Case 1.

the allowed range of  $\lambda_2$  varies only slightly around its electroweak value. On the contrary, allowed range for  $\lambda_1$  varies from 3 to 0.5 with the same variation in scale. In Figure 18(b), we have shown the region allowed after the constraints from  $g_\mu - 2$  and  $BR(h_{SM} \rightarrow AA)$  are applied. We have seen from our earlier discussions that  $g_\mu - 2$  favors large  $\tan\beta$  while the upper limit on  $BR(h_{SM} \rightarrow AA)$  favors low  $\tan\beta$ .  $\lambda_2$  is inversely proportional to  $\tan\beta$  in the alignment region. Therefore higher values of  $\lambda_2$  are disfavored by the observed  $g_\mu - 2$  data, while the lower  $\lambda_2$  gets constrained from the  $BR(h_{SM} \rightarrow AA)$ .

In Figure 18(c), we demonstrate regions with different levels of high-scale validity in the parameter space spanned by  $\lambda_1$  and  $\lambda_3$ . Their high-scale behavior appears to be strongly correlated with each other and the allowed range in the  $\lambda_1 - \lambda_3$  plane shows elliptic contours. Figure 18(d) shows the allowed region after the imposition of  $g_\mu - 2$  and  $BR(h_{SM} \rightarrow AA)$  constraints. We can see that these two constraints do not affect these couplings directly, but only reduces the density of points uniformly, depending on the other quartic couplings.

In Figure 18(e), we plot the high-scale validity in the  $\lambda_4 - \lambda_5$  plane. We have seen

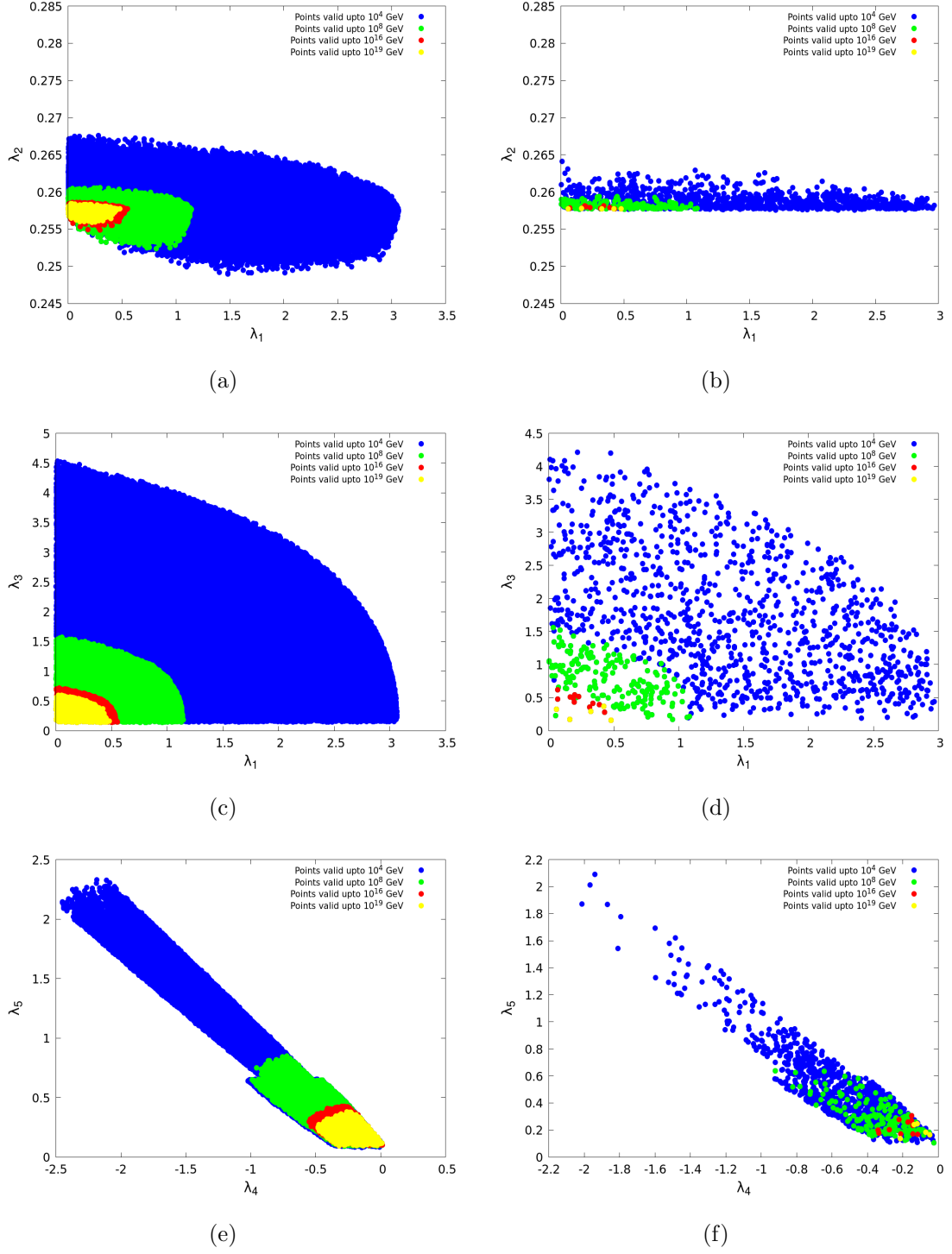


**Figure 18.** Quartic couplings valid upto different energy scales after applying (a),(c) and (e) theoretical constraints and (b),(d) and (f) theoretical constraints+ $(g_\mu-2)$  at  $3\sigma + BR(h_{SM} \rightarrow AA)$  bounds for Case 1.

in our earlier discussion that the mass degeneracy between  $m_H$  and  $m_{H^\pm}$  implies  $\lambda_4 \approx -\lambda_5$ . As the perturbative unitarity condition favors this mass degeneracy, this correlation between  $\lambda_4$  and  $\lambda_5$  is also favored for high-scale validity. The  $g_\mu - 2$  and  $\text{BR}(h_{SM} \rightarrow AA)$  constraints result in only uniform reduction of allowed points, the nature of the allowed region remaining unaltered (see Figure 18(f)).

It is clear from the discussion in the plane of quatic couplings that, the requirement of validity of the theory upto higher scales, pushes the quartic couplings to smaller values.

• **Case 2:**

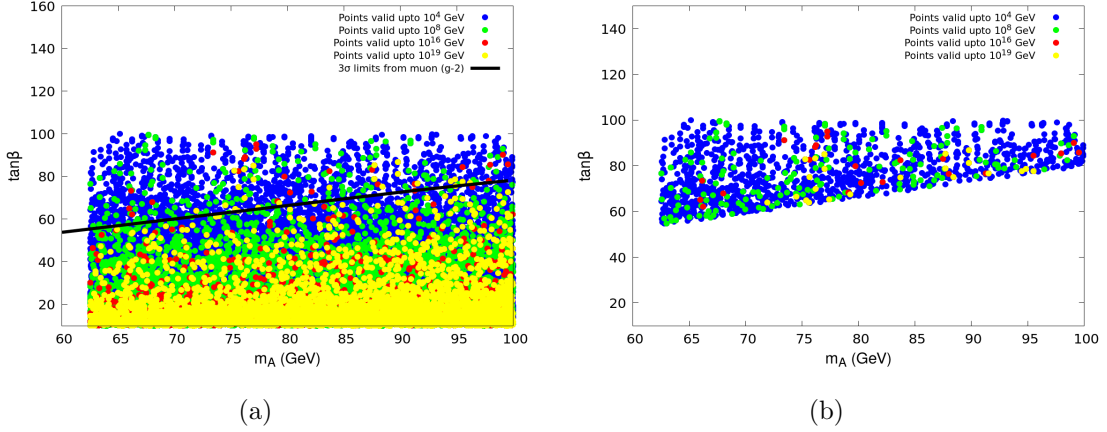


**Figure 19.**  $m_A - \tan \beta$  plane, valid upto different energy scales after applying (a) theoretical constraints (b) theoretical constraints +  $(g_\mu - 2)$  at  $3\sigma$  +  $\text{BR}(h_{SM} \rightarrow AA)$  bounds for Case 2.

In Figure 19, we show the high-scale validity in  $m_A - \tan \beta$  plane in the right-sign region of Scenario 1. Here the nature of high-scale validity is same as case 1 and for the same reason. The black line in the Figure 19(a) denotes the lower limit coming from the  $g_\mu - 2$  data. We have shown only the region  $m_A > \frac{m_h}{2}$  here, because from the upper limit on  $\text{BR}(h_{SM} \rightarrow AA)$ , this is the only allowed region in this case, as discussed in Section 5.

In Figure 20(a), (b) and (c) we show the high-scale validity in the  $(m_H - \tan \beta)$ ,  $(R_{(\beta-\alpha)} - \tan \beta)$  and  $(m_H - m_{H^\pm})$  planes respectively, after imposing the  $g_\mu - 2$  constraints and the upper limit from  $\text{BR}(h_{SM} \rightarrow AA)$ . Here too, we observe similar behavior as case 1 and the same discussion follows. We note here that,  $\tan \beta \lesssim 50$  is completely disfavored in this case unlike case 1. The reason behind this is in case 2, we do not have a region with  $m_A \lesssim \frac{m_h}{2}$  that satisfies the upper limit on  $\text{BR}(h_{SM} \rightarrow AA)$  and  $m_A > \frac{m_h}{2}$  region gets severely constrained by the lower limit from  $g_\mu - 2$  when  $\tan \beta \lesssim 50$ .

We report next on the high-scale validity in the RS region of Scenario 1 in the parameter space spanned by the quartic couplings. In Figure 21(a)-(f), we see similar features as in case 1. However, in this case, large values of  $\lambda_3$  become disfavored even at the electroweak scale as can be seen from Figure 21(c) and (d), since in the RS case a stronger upper bound is imposed on the  $m_{H^\pm}$  and  $m_H$ , compared to WS case, in the pseudoscalar mass range



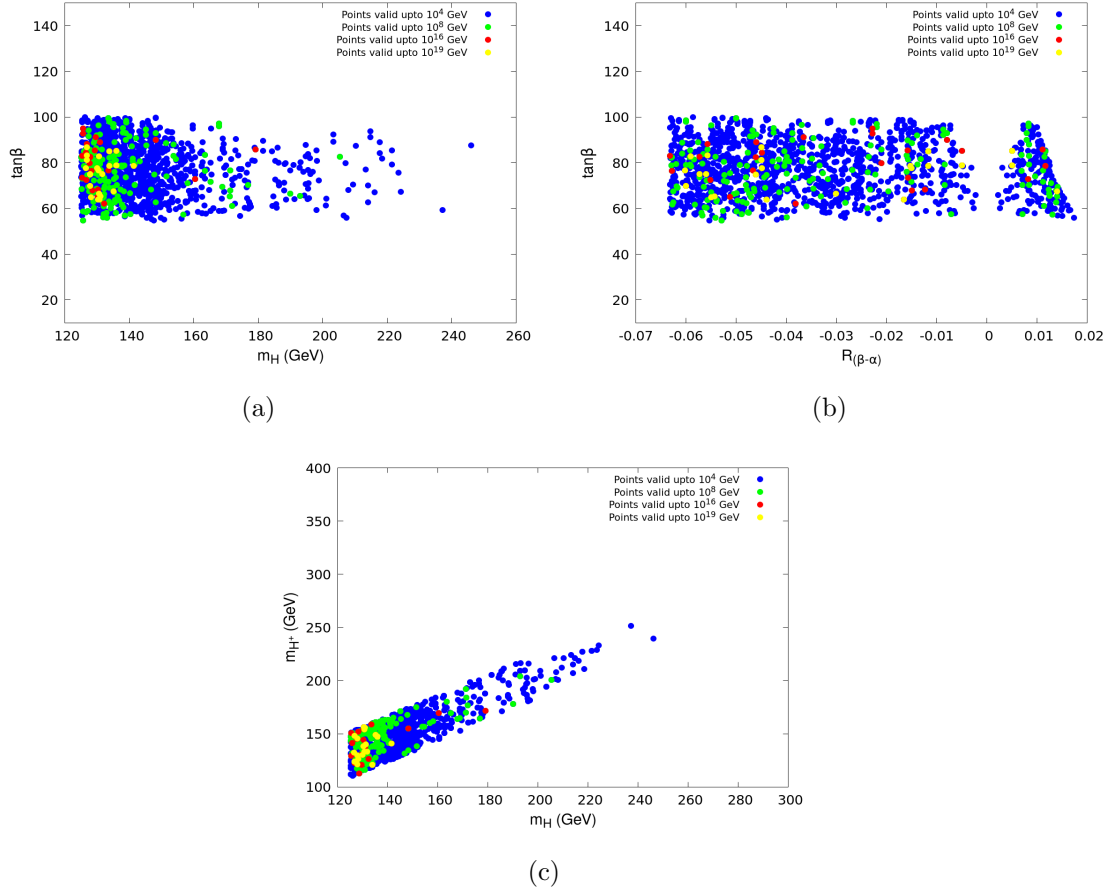


**Figure 20.** (a)  $m_H - \tan\beta$ , (b)  $R_{(\beta-\alpha)} - \tan\beta$  and (c)  $m_H - m_{H^\pm}$  plane, valid upto different energy scales after applying theoretical constraints +  $(g_\mu - 2)$  at  $3\sigma$  +  $BR(h_{SM} \rightarrow AA)$  bounds for Case 2.

of our interest. In Figure 21(e) and (f), we see, in this case, the lower masses of  $m_H$  and  $m_{H^\pm}$  restrict the upper limits on  $\lambda_4$  and  $\lambda_5$  to lower values compared to the WS case.

### • Case 3:

We now proceed to scenario 2 (ie.  $m_H = 125$  GeV), in the WS region. In Scenario 2, the charged scalar and the non-standard CP-even scalar masses are kept at a lower range compared to Scenario 1. In Figure 22, we show the the high-scale validity in the  $m_A - \tan\beta$  plane. Like the previous cases, here too, the tension between the high-scale validity and the observed  $g_\mu - 2$  continues. We have not shown the region  $m_A \lesssim \frac{m_H}{2}$  in Figure 22, because in Scenario 2, WS region, this region does not satisfy  $BR(h_{SM} \rightarrow AA)$  upper limit. On the other hand,  $m_A > \frac{m_H}{2}$  trivially satisfies this bound.

In Figure 23(a), (b) and (c), we show the parameter space allowed by all the aforementioned constraints in the  $(m_h - \tan\beta)$ ,  $(\sin(\beta - \alpha) - \tan\beta)$  and  $(m_h - m_{H^\pm})$  plane respectively. As a low mass range for the non-standard CP-even scalar ( $h$ ) is considered in this case, the entire mass range is valid upto very high scales. However, the  $g_\mu - 2$  data

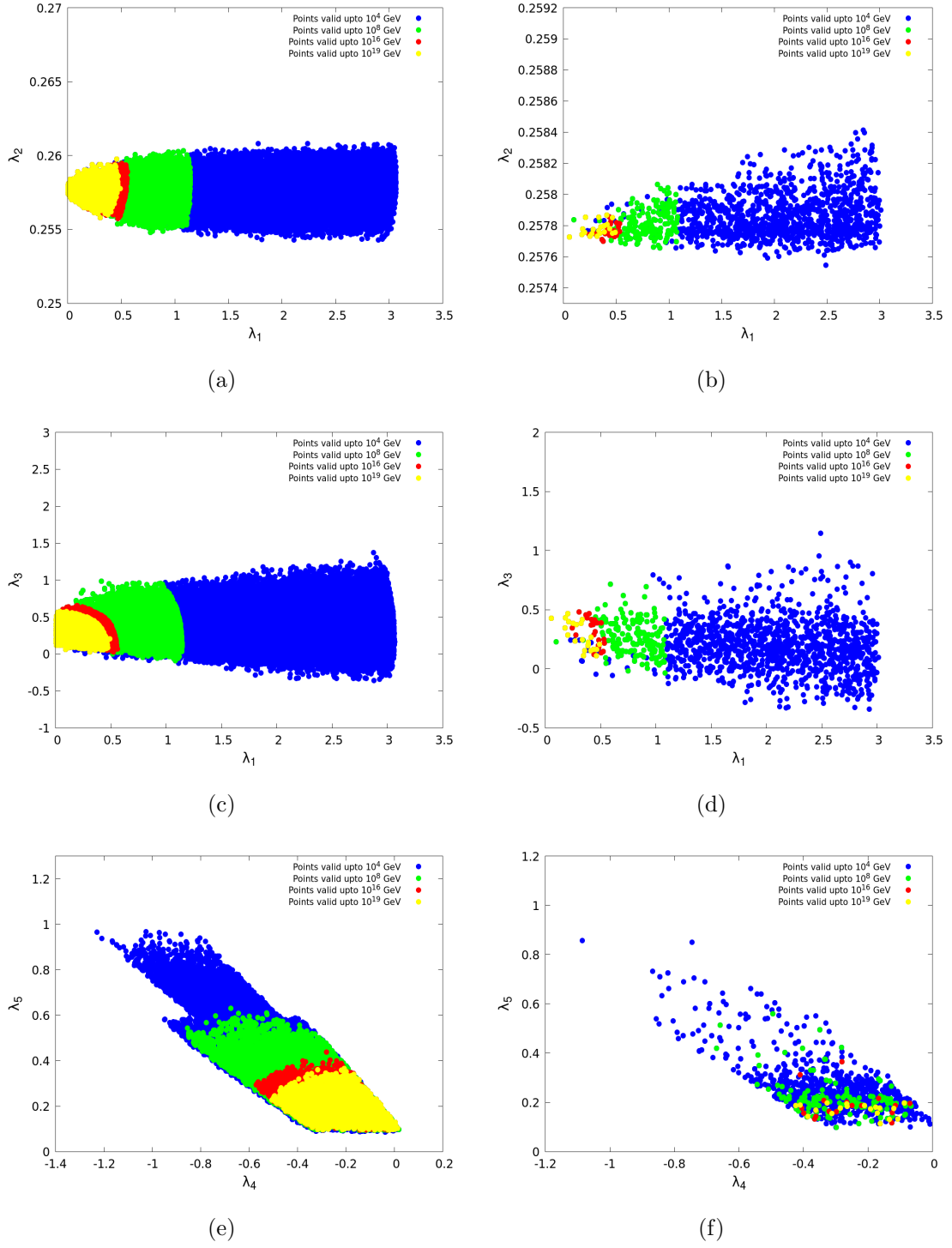


**Figure 21.** Quartic couplings valid upto different energy scales after applying (a),(c) and (e) theoretical constraints and (b),(d) and (f) theoretical constraints +  $(g_\mu - 2)$  at  $3\sigma$  +  $BR(h_{SM} \rightarrow AA)$  bounds for Case 2.

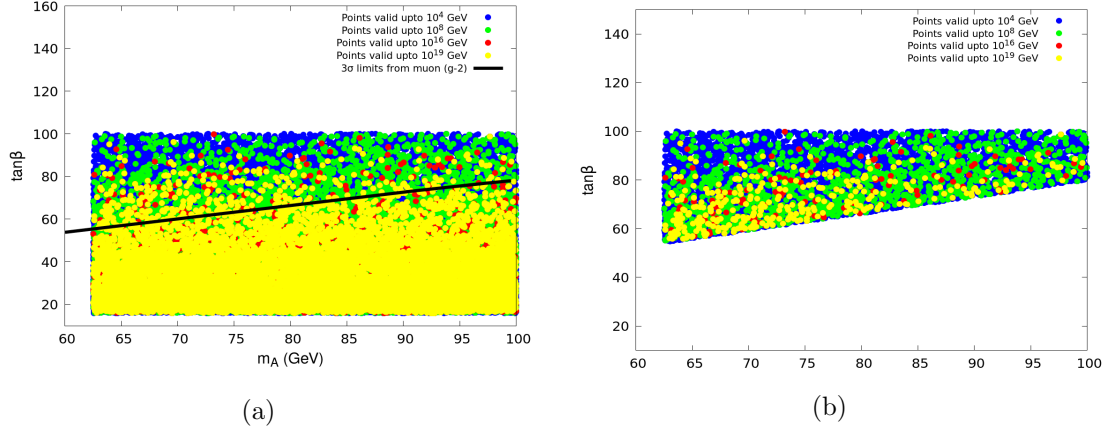


**Figure 22.**  $m_A - \tan\beta$  plane, valid upto different energy scales after applying (a) theoretical constraints (b) theoretical constraints +  $(g_\mu - 2)$  at  $3\sigma + BR(h_{SM} \rightarrow AA)$  bounds for Case 3.

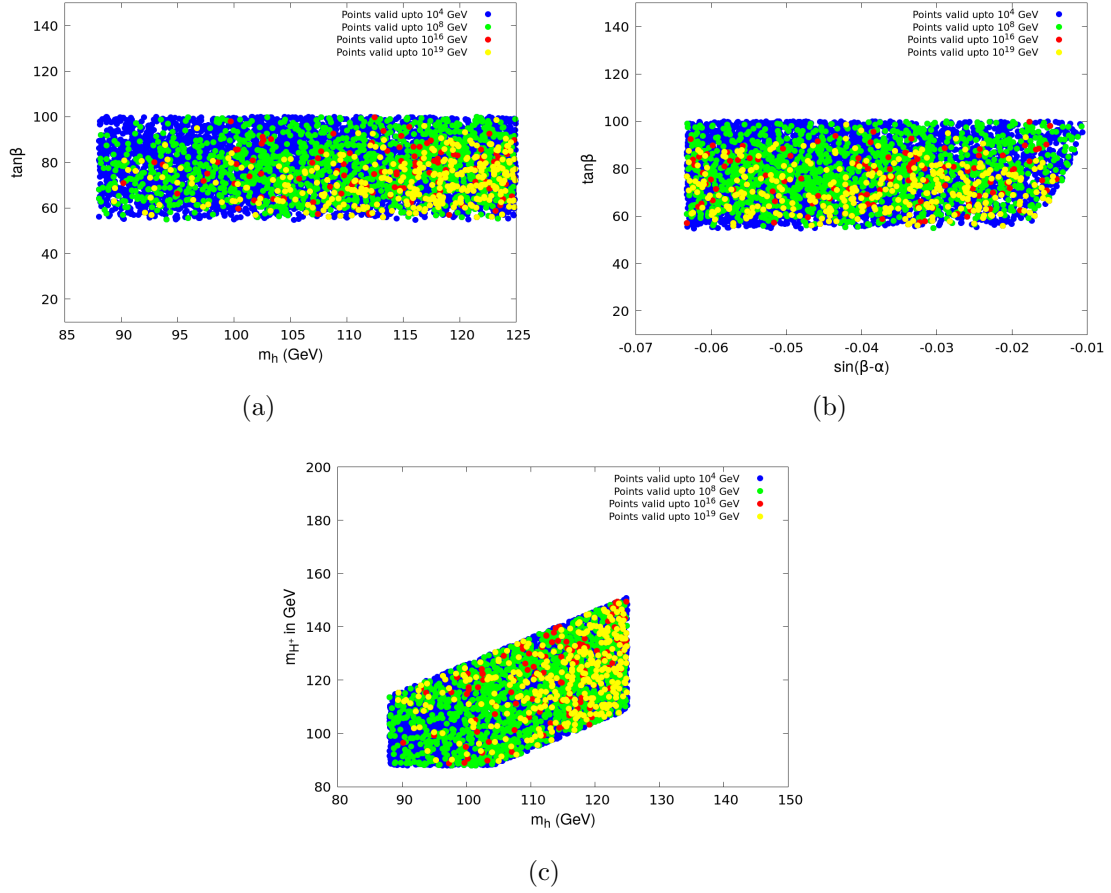


**Figure 23.** (a)  $m_h - \tan\beta$ , (b)  $\sin(\beta - \alpha) - \tan\beta$  and (c)  $m_h - m_{H^\pm}$  plane, valid upto different energy scales after applying theoretical constraints+  $(g_\mu - 2)$  at  $3\sigma + BR(h_{SM} \rightarrow AA)$  bounds for Case 3.

disfavors the region below  $\tan \beta \lesssim 50$  for  $m_A > \frac{m_h}{2}$  whereas  $m_A \lesssim \frac{m_h}{2}$  is disfavored from the upper limit on  $\text{BR}(h_{SM} \rightarrow AA)$ , therefore we see no point in the range  $\tan \beta \lesssim 50$  in Figure 23(a) and (b).

The behavior of the quartic couplings in the context of high-scale validity is similar to the previous cases considered, as we can see from Figure 24(a)-(f). The apparently stronger upper limit on  $\lambda_3$  in Figure 24(c) and (d) follows from the fact that the CP-even non-standard scalar mass ( $m_h$ ) is much lower in Scenario 2, compared to Scenario 1, irrespective of WS and RS. In Figure 24(e) and (f), we see a different behavior compared to scenario 1. The correlation between  $\lambda_4$  and  $\lambda_5$  here is not very clear. The reason again being, in Scenario 2, we are confined within small range for  $m_h$  and therefore the degeneracy, which is responsible for the correlation between  $\lambda_4$  and  $\lambda_5$ , is not very apparent in this case. As the non-standard scalar masses are already small, almost the entire region considered is allowed upto a very high scale ( $10^{19}$  GeV).

#### • Case 4:

Now we will focus on the RS region of scenario 2 ie.  $m_H = 125$  GeV. Here too, the charged Higgs and the non-standard CP-even scalar masses are kept on the lower side. In Figure 25, similar behavior as the previous cases is observed. One may note, similar to case 1, here we get a small region in the range  $m_A \lesssim \frac{m_H}{2}$ , mostly in the low  $\tan \beta$ , which satisfies the constraint from  $\text{BR}(h_{SM} \rightarrow AA)$ .

In Figure 26(a), (b) and (c), we show the allowed parameter space in the plane spanned by  $(m_h - \tan \beta)$ ,  $(\sin(\beta - \alpha) - \tan \beta)$  and  $(m_h - m_{H^\pm})$  plane respectively. Due to low mass range of the non-standard scalars, the entire mass range considered is valid upto very high scales just like in case 3. The strip below  $\tan \beta \lesssim 50$  in Figure 26(a) and (b) corresponds to the points with  $m_A \lesssim \frac{m_H}{2}$ , that satisfy the limit from  $\text{BR}(h_{SM} \rightarrow AA)$ , as we have argued in case 1.

Next we show the region of parameter space in the plane of the quartic couplings, in Figure 27(a)-(f). The qualitative nature of the allowed regions are very similar to case 3, precisely because of low non-standard scalar masses in both cases.

The most salient points of the discussion in the current section can be summarized as follows:

- Irrespective of the specific case at hand, the smaller the quartic couplings are at the electroweak scale, the higher is the scale of validity of a theory.
- The requirement of small quartic couplings naturally implies moderate  $\tan \beta$  and/or non-standard scalar masses on the lower side.
- The observed  $g_\mu - 2$  data favor large  $\tan \beta$ , creating a tension with high-scale validity.
- $\lambda_1$  (also  $\lambda_3$ , although in a correlated manner with  $\lambda_1$ ) and  $\lambda_5$  ( $\lambda_4$  shows a strong correlation with it), mainly control the high-scale behavior and remain practically unaffected by the constraints such as  $g_\mu - 2$  or the  $\text{BR}(h_{SM} \rightarrow AA)$ .

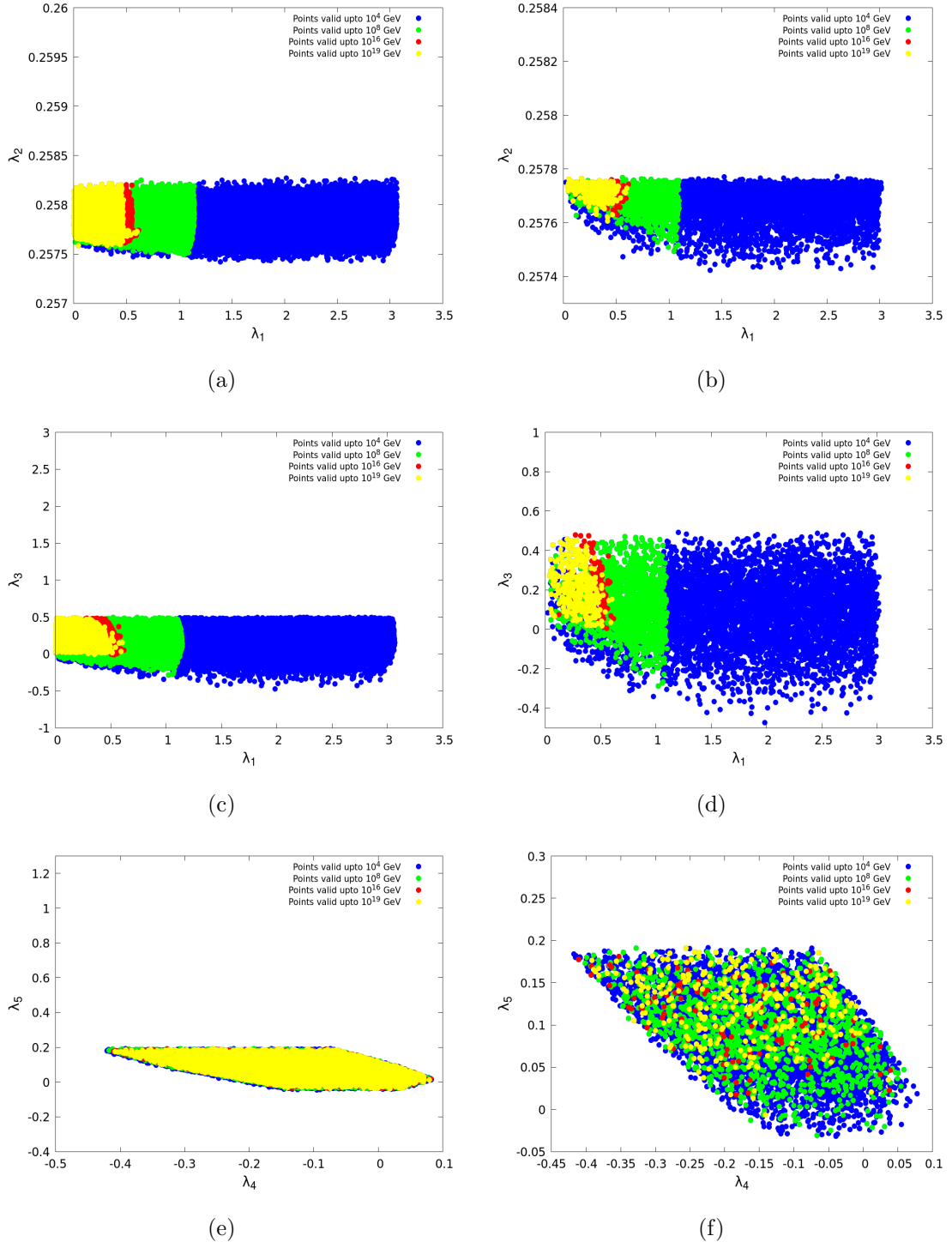


**Figure 24.** Quartic couplings valid upto different energy scales after applying (a),(c) and (e) theoretical constraints and (b),(d) and (f) theoretical constraints +  $(g_\mu - 2)$  at  $3\sigma$  +  $BR(h_{SM} \rightarrow AA)$  bounds for Case 3.

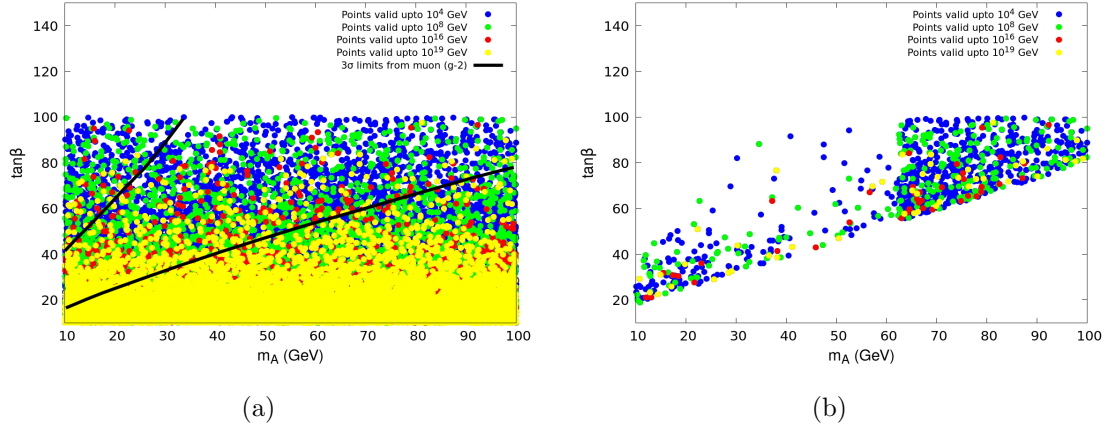


**Figure 25.**  $m_A - \tan\beta$  plane, valid upto different energy scales after applying (a) theoretical constraints (b) theoretical constraints +  $(g_\mu - 2)$  at  $3\sigma$  +  $BR(h_{SM} \rightarrow AA)$  bounds for Case 4.

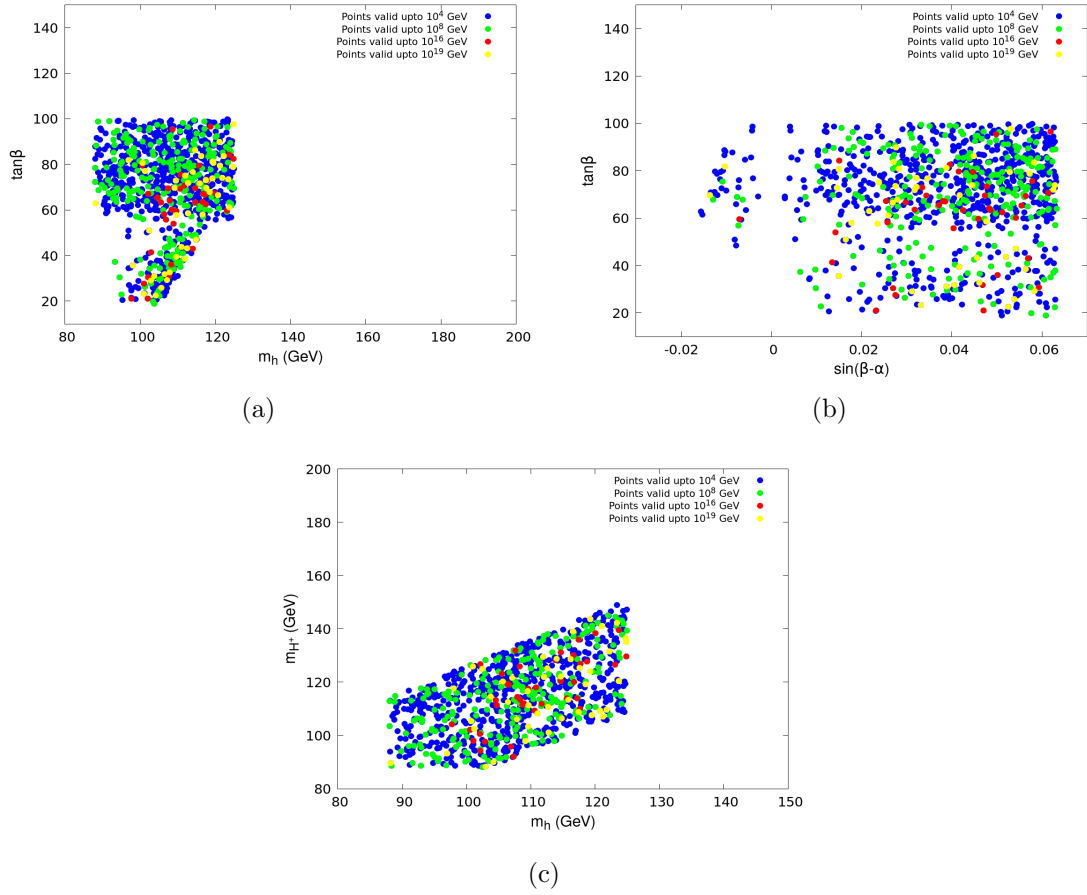


**Figure 26.** (a)  $m_h - \tan\beta$ , (b)  $\sin(\beta - \alpha) - \tan\beta$  and (c)  $m_h - m_{H^\pm}$  plane, valid upto different energy scales after applying theoretical constraints +  $(g_\mu - 2)$  at  $3\sigma$  +  $BR(h_{SM} \rightarrow AA)$  bounds for Case 4.

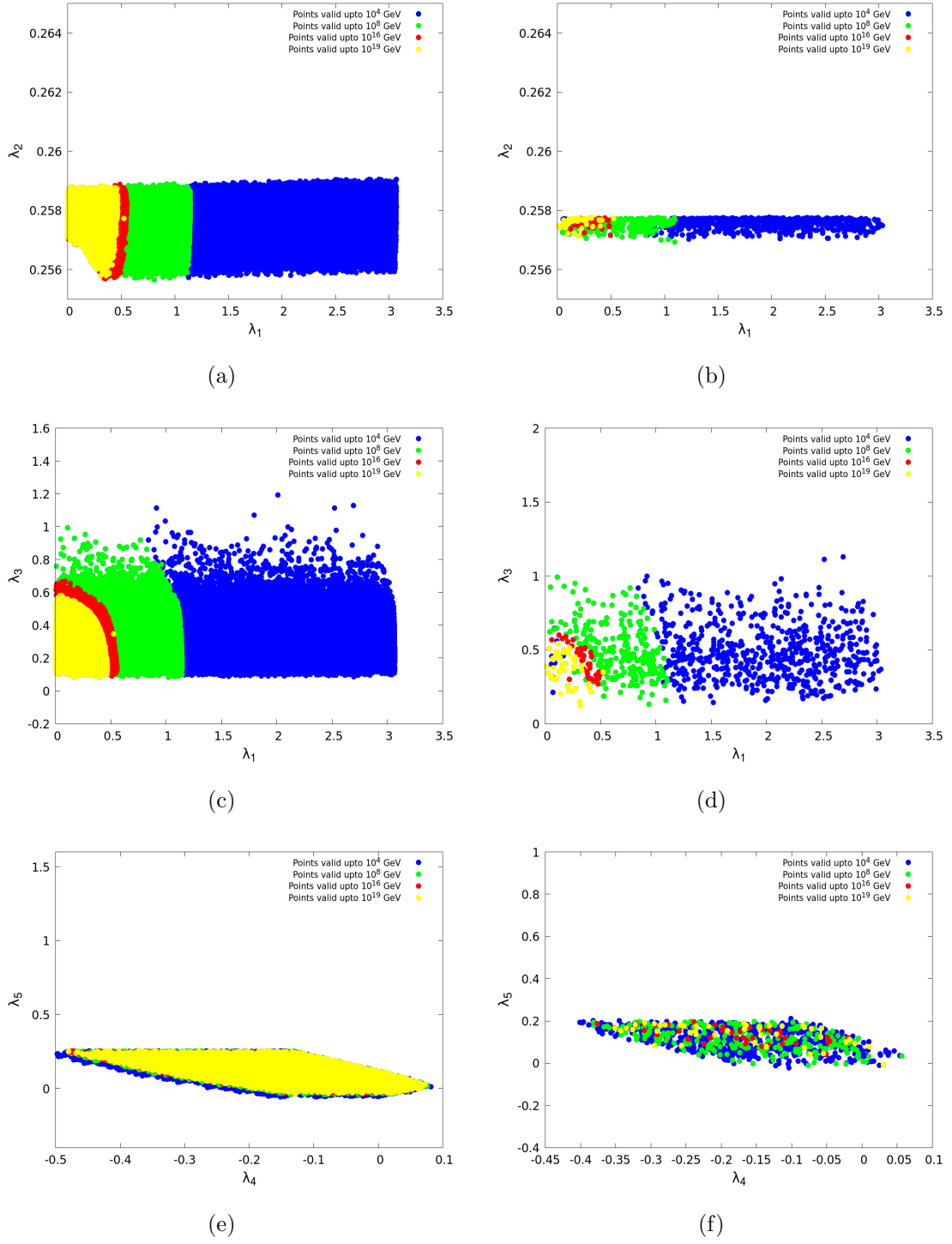


**Figure 27.** Quartic couplings valid upto different energy scales after applying (a),(c) and (e) theoretical constraints and (b),(d) and (f) theoretical constraints +  $(g_\mu - 2)$  at  $3\sigma$  +  $BR(h_{SM} \rightarrow AA)$  bounds for Case 4.

- $\lambda_2$  on the other hand, does not play a significant role in the high-scale validity, but remains heavily constrained from  $g_\mu - 2$  and  $\text{BR}(h_{SM} \rightarrow AA)$ .
- High-scale validity in general demands degeneracy between the non-standard scalar masses as well as their closeness to the 125-GeV Higgs mass.
- In case 2, ie. when the lighter CP-even scalar is SM-like in the right-sign region, the requirement of perturbative unitarity at the electroweak scale, already favors lower non-standard scalar masses and consequently lower quartic couplings, facilitating high-scale validity.
- In Scenario 2 (both cases 3 and 4), the non-standard scalar masses are on the lower side, as compared to Scenario 1. Therefore, here too, a major portion of the parameter space remains valid upto Planck scale.
- Case 1 is least favored among the four cases considered, when high-scale validity is demanded.

## 7 Conclusion

We have explored the high-scale validity of Type-X 2HDM, particularly in regions of the parameter space answering to a low-mass neutral CP-odd spinless particle. Such a pseudoscalar is not only consistent with all experimental limits so far but can also help in explaining the observed discrepancy in  $g_\mu - 2$ . The high-scale validity of the regions of the parameter space of this model, where the above features of special interest are noticed, has been studied here.

We have identified the regions in the parameter space, which are helpful in explaining  $(g_\mu - 2)$  including the most recent results. Other theoretical and experimental constraints, starting from low-scale perturbative unitarity, vacuum stability etc., and all the way to the most recent LHC limits, have been used to filter out the surviving parameter regions. The two-loop running of various couplings in such regions upto high scales has been studied thereafter, thus identifying regions where perturbative unitarity and vacuum stability are satisfied upto various high scales, ranging from  $10^4$  GeV to the Planck scale. Different benchmark points have been used, including both situations where the 125-GeV state is either the lighter or the heavier neutral CP-even scalar. Scenarios with both right- and wrong-sign Yukawa couplings have also scanned across the parameter space.

For regions in the parameter space having cut-off scales on the lower side, the aspiration for perturbative unification of the three SM gauge couplings is found to necessitate UV completion of Type-X 2HDM below the GUT scale. For regions with perturbative validity inching up to the Planck scale, on the other hand, the requirements for gauge coupling unification turn out to be similar to what they are for the standard model electroweak symmetry breaking sector. All this bears ample testimony to the Type-X 2HDM being a candidate theory that explains the observed value of  $g_\mu - 2$ , keeping open a rich set of UV completion possibilities.



## 8 Acknowledgements

We thank Amitava Raychaudhuri for useful discussions. This work was partially supported by funding available from the Department of Atomic Energy, Government of India, for the Regional Centre for Accelerator-based Particle Physics (RECAPP), Harish-Chandra Research Institute. BM would like to thank RECAPP, HRI, where significant part of the work was done. AD and JL would like to thank Indian Institute of Science Education and Research, Kolkata, where part of the work was done.

## References

- [1] MUON G-2 collaboration, G. W. Bennett et al., *Final Report of the Muon E821 Anomalous Magnetic Moment Measurement at BNL*, *Phys. Rev.* **D73** (2006) 072003, [[hep-ex/0602035](#)].
- [2] MUON G-2 collaboration, B. Abi et al., *Measurement of the Positive Muon Anomalous Magnetic Moment to 0.46 ppm*, *Phys. Rev. Lett.* **126** (2021) 141801, [[2104.03281](#)].
- [3] MUON G-2 collaboration, T. Albahri et al., *Measurement of the anomalous precession frequency of the muon in the Fermilab Muon  $g - 2$  Experiment*, *Phys. Rev.* **D103** (2021) 072002, [[2104.03247](#)].
- [4] A. Arhrib, C.-W. Chiang, D. K. Ghosh and R. Santos, *Two Higgs Doublet Model in light of the Standard Model  $H \rightarrow \tau^+\tau^-$  search at the LHC*, *Phys. Rev. D* **85** (2012) 115003, [[1112.5527](#)].
- [5] X. Liu, L. Bian, X.-Q. Li and J. Shu, *Type-III two Higgs doublet model plus a pseudoscalar confronted with  $h \rightarrow \mu\tau$ , muon  $g - 2$  and dark matter*, *Nucl. Phys.* **B909** (2016) 507–524, [[1508.05716](#)].
- [6] E. J. Chun, S. Dwivedi, T. Mondal and B. Mukhopadhyaya, *Reconstructing a light pseudoscalar in the Type-X Two Higgs Doublet Model*, *Phys. Lett.* **B774** (2017) 20–25, [[1707.07928](#)].
- [7] E. J. Chun, S. Dwivedi, T. Mondal, B. Mukhopadhyaya and S. K. Rai, *Reconstructing heavy Higgs boson masses in a type X two-Higgs-doublet model with a light pseudoscalar particle*, *Phys. Rev.* **D98** (2018) 075008, [[1807.05379](#)].
- [8] N. Chakrabarty, C.-W. Chiang, T. Ohata and K. Tsumura, *Charged scalars confronting neutrino mass and muon  $g - 2$  anomaly*, *JHEP* **12** (2018) 104, [[1807.08167](#)].
- [9] S. Iguro, Y. Omura and M. Takeuchi, *Testing the 2HDM explanation of the muon  $g - 2$  anomaly at the LHC*, *JHEP* **11** (2019) 130, [[1907.09845](#)].
- [10] E. J. Chun, J. Kim and T. Mondal, *Electron EDM and Muon anomalous magnetic moment in Two-Higgs-Doublet Models*, *JHEP* **12** (2019) 068, [[1906.00612](#)].
- [11] P. Bandyopadhyay, E. J. Chun and R. Mandal, *Phenomenology of Higgs bosons in inverse seesaw model with Type-X two Higgs doublet at the LHC*, *JHEP* **08** (2019) 169, [[1904.09494](#)].
- [12] M. Frank and I. Saha, *Muon Anomalous Magnetic Moment in Two Higgs Doublet Models with Vector-Like Leptons*, [2008.11909](#).
- [13] J. E. Chun and T. Mondal, *Explaining  $g - 2$  anomalies in two Higgs doublet model with vector-like leptons*, [2009.08314](#).

- [14] A. Jueid, J. Kim, S. Lee and J. Song, *Type-X two Higgs doublet model in light of the muon  $g - 2$ : confronting Higgs and collider data*, [2104.10175](#).
- [15] G. C. Branco, P. M. Ferreira, L. Lavoura, M. N. Rebelo, M. Sher and J. P. Silva, *Theory and phenomenology of two-Higgs-doublet models*, *Phys. Rept.* **516** (2012) 1–102, [[1106.0034](#)].
- [16] X.-F. Han and H.-X. Wang, *Revisiting wrong sign Yukawa coupling of type II two-Higgs-doublet model in light of recent LHC data*, *Chin. Phys. C* **44** (2020) 073101, [[2003.06170](#)].
- [17] CMS collaboration, A. M. Sirunyan et al., *Combined measurements of Higgs boson couplings in proton–proton collisions at  $\sqrt{s} = 13$  TeV*, *Eur. Phys. J.* **C79** (2019) 421, [[1809.10733](#)].
- [18] ATLAS collaboration, G. Aad et al., *Combined measurements of Higgs boson production and decay using up to 80  $\text{fb}^{-1}$  of proton-proton collision data at  $\sqrt{s} = 13$  TeV collected with the ATLAS experiment*, *Phys. Rev.* **D101** (2020) 012002, [[1909.02845](#)].
- [19] T. Blum, A. Denig, I. Logashenko, E. de Rafael, B. L. Roberts, T. Teubner et al., *The Muon ( $g-2$ ) Theory Value: Present and Future*, [1311.2198](#).
- [20] J-PARC MUON  $G-2$ /EDM collaboration, H. Inuma, *New approach to the muon  $g-2$  and EDM experiment at J-PARC*, *J. Phys. Conf. Ser.* **295** (2011) 012032.
- [21] M. Davier, A. Hoecker, B. Malaescu and Z. Zhang, *Reevaluation of the Hadronic Contributions to the Muon  $g-2$  and to  $\alpha(M_Z)$* , *Eur. Phys. J.* **C71** (2011) 1515, [[1010.4180](#)].
- [22] K. Hagiwara, R. Liao, A. D. Martin, D. Nomura and T. Teubner,  *$(g - 2)_\mu$  and  $\alpha(M_Z^2)$  re-evaluated using new precise data*, *J. Phys.* **G38** (2011) 085003, [[1105.3149](#)].
- [23] M. Davier, A. Hoecker, B. Malaescu and Z. Zhang, *Reevaluation of the hadronic vacuum polarisation contributions to the Standard Model predictions of the muon  $g - 2$  and  $\alpha(m_Z^2)$  using newest hadronic cross-section data*, *Eur. Phys. J.* **C77** (2017) 827, [[1706.09436](#)].
- [24] M. Davier, A. Hoecker, B. Malaescu and Z. Zhang, *A new evaluation of the hadronic vacuum polarisation contributions to the muon anomalous magnetic moment and to  $\alpha(m_Z^2)$* , *Eur. Phys. J.* **C80** (2020) 241, [[1908.00921](#)].
- [25] T. Aoyama et al., *The anomalous magnetic moment of the muon in the Standard Model*, [2006.04822](#).
- [26] A. Keshavarzi, D. Nomura and T. Teubner, *Muon  $g - 2$  and  $\alpha(M_Z^2)$ : a new data-based analysis*, *Phys. Rev. D* **97** (2018) 114025, [[1802.02995](#)].
- [27] G. Colangelo, M. Hoferichter and P. Stoffer, *Two-pion contribution to hadronic vacuum polarization*, *JHEP* **02** (2019) 006, [[1810.00007](#)].
- [28] M. Hoferichter, B.-L. Hoid and B. Kubis, *Three-pion contribution to hadronic vacuum polarization*, *JHEP* **08** (2019) 137, [[1907.01556](#)].
- [29] A. Keshavarzi, D. Nomura and T. Teubner,  *$g - 2$  of charged leptons,  $\alpha(M_Z^2)$ , and the hyperfine splitting of muonium*, *Phys. Rev. D* **101** (2020) 014029, [[1911.00367](#)].
- [30] A. Kurz, T. Liu, P. Marquard and M. Steinhauser, *Hadronic contribution to the muon anomalous magnetic moment to next-to-next-to-leading order*, *Phys. Lett. B* **734** (2014) 144–147, [[1403.6400](#)].
- [31] K. Melnikov and A. Vainshtein, *Hadronic light-by-light scattering contribution to the muon anomalous magnetic moment revisited*, *Phys. Rev. D* **70** (2004) 113006, [[hep-ph/0312226](#)].

- [32] P. Masjuan and P. Sanchez-Puertas, *Pseudoscalar-pole contribution to the  $(g_\mu - 2)$ : a rational approach*, *Phys. Rev. D* **95** (2017) 054026, [[1701.05829](#)].
- [33] G. Colangelo, M. Hoferichter, M. Procura and P. Stoffer, *Dispersion relation for hadronic light-by-light scattering: two-pion contributions*, *JHEP* **04** (2017) 161, [[1702.07347](#)].
- [34] M. Hoferichter, B.-L. Hoid, B. Kubis, S. Leupold and S. P. Schneider, *Dispersion relation for hadronic light-by-light scattering: pion pole*, *JHEP* **10** (2018) 141, [[1808.04823](#)].
- [35] A. Gérardin, H. B. Meyer and A. Nyffeler, *Lattice calculation of the pion transition form factor with  $N_f = 2 + 1$  Wilson quarks*, *Phys. Rev. D* **100** (2019) 034520, [[1903.09471](#)].
- [36] J. Bijnens, N. Hermansson-Truedsson and A. Rodríguez-Sánchez, *Short-distance constraints for the  $HLbL$  contribution to the muon anomalous magnetic moment*, *Phys. Lett. B* **798** (2019) 134994, [[1908.03331](#)].
- [37] G. Colangelo, F. Hagelstein, M. Hoferichter, L. Laub and P. Stoffer, *Longitudinal short-distance constraints for the hadronic light-by-light contribution to  $(g - 2)_\mu$  with large- $N_c$  Regge models*, *JHEP* **03** (2020) 101, [[1910.13432](#)].
- [38] G. Colangelo, M. Hoferichter, A. Nyffeler, M. Passera and P. Stoffer, *Remarks on higher-order hadronic corrections to the muon  $g-2$* , *Phys. Lett. B* **735** (2014) 90–91, [[1403.7512](#)].
- [39] T. Blum, N. Christ, M. Hayakawa, T. Izubuchi, L. Jin, C. Jung et al., *Hadronic Light-by-Light Scattering Contribution to the Muon Anomalous Magnetic Moment from Lattice QCD*, *Phys. Rev. Lett.* **124** (2020) 132002, [[1911.08123](#)].
- [40] T. Aoyama, M. Hayakawa, T. Kinoshita and M. Nio, *Complete Tenth-Order QED Contribution to the Muon  $g-2$* , *Phys. Rev. Lett.* **109** (2012) 111808, [[1205.5370](#)].
- [41] A. Czarnecki, W. J. Marciano and A. Vainshtein, *Refinements in electroweak contributions to the muon anomalous magnetic moment*, *Phys. Rev. D* **67** (2003) 073006, [[hep-ph/0212229](#)].
- [42] T. Aoyama, T. Kinoshita and M. Nio, *Theory of the Anomalous Magnetic Moment of the Electron*, *Atoms* **7** (2019) 28.
- [43] C. Gnendiger, D. Stöckinger and H. Stöckinger-Kim, *The electroweak contributions to  $(g - 2)_\mu$  after the Higgs boson mass measurement*, *Phys. Rev. D* **88** (2013) 053005, [[1306.5546](#)].
- [44] PARTICLE DATA GROUP collaboration, P. A. Zyla et al., *Review of Particle Physics*, *PTEP* **2020** (2020) 083C01.
- [45] F. S. Queiroz and W. Shepherd, *New Physics Contributions to the Muon Anomalous Magnetic Moment: A Numerical Code*, *Phys. Rev.* **D89** (2014) 095024, [[1403.2309](#)].
- [46] V. Ilisie, *New Barr-Zee contributions to  $(g - 2)_\mu$  in two-Higgs-doublet models*, *JHEP* **04** (2015) 077, [[1502.04199](#)].
- [47] A. Broggio, E. J. Chun, M. Passera, K. M. Patel and S. K. Vempati, *Limiting two-Higgs-doublet models*, *JHEP* **11** (2014) 058, [[1409.3199](#)].
- [48] A. Cherchiglia, D. Stöckinger and H. Stöckinger-Kim, *Muon  $g-2$  in the 2HDM: maximum results and detailed phenomenology*, *Phys. Rev. D* **98** (2018) 035001, [[1711.11567](#)].
- [49] GFITTER collaboration, M. Baak, *Review of electroweak fits of the SM and beyond, after the Higgs discovery – with Gfitter*, *PoS EPS-HEP2013* (2013) 203.

- [50] J. Haller, A. Hoecker, R. Kogler, K. Mönig, T. Peiffer and J. Stelzer, *Update of the global electroweak fit and constraints on two-Higgs-doublet models*, *Eur. Phys. J.* **C78** (2018) 675, [[1803.01853](#)].
- [51] A. Crivellin, A. Kokulu and C. Greub, *Flavor-phenomenology of two-Higgs-doublet models with generic Yukawa structure*, *Phys. Rev.* **D87** (2013) 094031, [[1303.5877](#)].
- [52] A. Arbey, F. Mahmoudi, O. Stal and T. Stefaniak, *Status of the Charged Higgs Boson in Two Higgs Doublet Models*, *Eur. Phys. J.* **C78** (2018) 182, [[1706.07414](#)].
- [53] M. Hussain, M. Usman, M. A. Paracha and M. J. Aslam, *Constraints on Two Higgs Doublet Model Parameters in the light of rare B-Decays*, *Phys. Rev.* **D95** (2017) 075009, [[1703.10845](#)].
- [54] D. A. Dicus and V. S. Mathur, *Upper bounds on the values of masses in unified gauge theories*, *Phys. Rev.* **D7** (1973) 3111–3114.
- [55] B. W. Lee, C. Quigg and H. B. Thacker, *The Strength of Weak Interactions at Very High-Energies and the Higgs Boson Mass*, *Phys. Rev. Lett.* **38** (1977) 883–885.
- [56] N. G. Deshpande and E. Ma, *Pattern of Symmetry Breaking with Two Higgs Doublets*, *Phys. Rev.* **D18** (1978) 2574.
- [57] S. Nie and M. Sher, *Vacuum stability bounds in the two Higgs doublet model*, *Phys. Lett.* **B449** (1999) 89–92, [[hep-ph/9811234](#)].
- [58] J. F. Gunion and H. E. Haber, *The CP conserving two Higgs doublet model: The Approach to the decoupling limit*, *Phys. Rev.* **D67** (2003) 075019, [[hep-ph/0207010](#)].
- [59] P. M. Ferreira, J. F. Gunion, H. E. Haber and R. Santos, *Probing wrong-sign Yukawa couplings at the LHC and a future linear collider*, *Phys. Rev.* **D89** (2014) 115003, [[1403.4736](#)].
- [60] ALEPH, DELPHI, L3, OPAL, LEP collaboration, G. Abbiendi et al., *Search for Charged Higgs bosons: Combined Results Using LEP Data*, *Eur. Phys. J.* **C73** (2013) 2463, [[1301.6065](#)].
- [61] DELPHI collaboration, J. Abdallah et al., *Searches for neutral higgs bosons in extended models*, *Eur. Phys. J.* **C38** (2004) 1–28, [[hep-ex/0410017](#)].
- [62] S. Kanemura, K. Tsumura and H. Yokoya, *Multi-tau-lepton signatures at the LHC in the two Higgs doublet model*, *Phys. Rev.* **D85** (2012) 095001, [[1111.6089](#)].
- [63] S. Kanemura, K. Tsumura, K. Yagyu and H. Yokoya, *Fingerprinting nonminimal Higgs sectors*, *Phys. Rev.* **D90** (2014) 075001, [[1406.3294](#)].
- [64] CMS collaboration, A. M. Sirunyan et al., *Search for an exotic decay of the Higgs boson to a pair of light pseudoscalars in the final state of two muons and two  $\tau$  leptons in proton-proton collisions at  $\sqrt{s} = 13$  TeV*, *JHEP* **11** (2018) 018, [[1805.04865](#)].
- [65] J. Bernon, J. F. Gunion, Y. Jiang and S. Kraml, *Light Higgs bosons in Two-Higgs-Doublet Models*, *Phys. Rev.* **D91** (2015) 075019, [[1412.3385](#)].
- [66] CMS collaboration, V. Khachatryan et al., *Search for a Low-Mass Pseudoscalar Higgs Boson Produced in Association with a  $b\bar{b}$  Pair in pp Collisions at  $\sqrt{s} = 8$  TeV*, *Phys. Lett.* **B758** (2016) 296–320, [[1511.03610](#)].
- [67] CMS collaboration, A. M. Sirunyan et al., *Search for a low-mass  $\tau^+\tau^-$  resonance in*

association with a bottom quark in proton-proton collisions at  $\sqrt{s} = 13$  TeV, *JHEP* **05** (2019) 210, [[1903.10228](#)].

- [68] CMS collaboration, V. Khachatryan et al., *Search for neutral MSSM Higgs bosons decaying into a pair of bottom quarks*, *JHEP* **11** (2015) 071, [[1506.08329](#)].
- [69] CMS collaboration, C. Collaboration, *Search for a narrow heavy decaying to bottom quark pairs in the 13 TeV data sample*, CMS-PAS-HIG-16-025, .
- [70] CMS collaboration, V. Khachatryan et al., *Search for neutral resonances decaying into a Z boson and a pair of b jets or  $\tau$  leptons*, *Phys. Lett.* **B759** (2016) 369–394, [[1603.02991](#)].
- [71] CMS collaboration, C. Collaboration, *Search for  $H$  to  $Z(\ell\ell)+A(bb)$  with 2015 data*, CMS-PAS-HIG-16-010, .
- [72] CMS collaboration, A. M. Sirunyan et al., *Search for resonant pair production of Higgs bosons decaying to bottom quark-antiquark pairs in proton-proton collisions at 13 TeV*, *JHEP* **08** (2018) 152, [[1806.03548](#)].
- [73] CMS collaboration, A. M. Sirunyan et al., *Search for Higgs boson pair production in the  $\gamma\gamma b\bar{b}$  final state in pp collisions at  $\sqrt{s} = 13$  TeV*, *Phys. Lett.* **B788** (2019) 7–36, [[1806.00408](#)].
- [74] ATLAS collaboration, M. Aaboud et al., *Search for pair production of Higgs bosons in the  $b\bar{b}b\bar{b}$  final state using proton-proton collisions at  $\sqrt{s} = 13$  TeV with the ATLAS detector*, *JHEP* **01** (2019) 030, [[1804.06174](#)].
- [75] ATLAS collaboration, T. A. collaboration, *Search for a high-mass Higgs boson decaying to a pair of W bosons in pp collisions at  $\sqrt{s}=13$  TeV with the ATLAS detector*, .
- [76] T. A. collaboration, *Search for high-mass resonances decaying into a Z boson pair in the  $\ell\ell\nu\nu$  final state in pp collisions at  $\sqrt{s} = 13$  TeV with the ATLAS detector*, .
- [77] ATLAS collaboration, G. Aad et al., *Search for resonances decaying into photon pairs in  $139\text{ fb}^{-1}$  of pp collisions at  $\sqrt{s} = 13$  TeV with the ATLAS detector*, **2102.13405**.
- [78] ATLAS collaboration, G. Aad et al., *Search for charged Higgs bosons decaying via  $H^\pm \rightarrow \tau^\pm\nu$  in fully hadronic final states using pp collision data at  $\sqrt{s} = 8$  TeV with the ATLAS detector*, *JHEP* **03** (2015) 088, [[1412.6663](#)].
- [79] CMS collaboration, V. Khachatryan et al., *Search for a charged Higgs boson in pp collisions at  $\sqrt{s} = 8$  TeV*, *JHEP* **11** (2015) 018, [[1508.07774](#)].
- [80] ATLAS collaboration, G. Aad et al., *Search for a light charged Higgs boson in the decay channel  $H^\pm \rightarrow c\bar{s}$  in  $t\bar{t}$  events using pp collisions at  $\sqrt{s} = 7$  TeV with the ATLAS detector*, *Eur. Phys. J.* **C73** (2013) 2465, [[1302.3694](#)].
- [81] CMS collaboration, V. Khachatryan et al., *Search for a light charged Higgs boson decaying to  $c\bar{s}$  in pp collisions at  $\sqrt{s} = 8$  TeV*, *JHEP* **12** (2015) 178, [[1510.04252](#)].
- [82] ATLAS collaboration, M. Aaboud et al., *Search for charged Higgs bosons produced in association with a top quark and decaying via  $H^\pm \rightarrow \tau\nu$  using pp collision data recorded at  $\sqrt{s} = 13$  TeV by the ATLAS detector*, *Phys. Lett.* **B759** (2016) 555–574, [[1603.09203](#)].
- [83] ATLAS collaboration, T. A. collaboration, *Search for charged Higgs bosons in the  $\tau$ +jets final state using  $14.7\text{ fb}^{-1}$  of pp collision data recorded at of pp collision data recorded at  $\sqrt{s}=13$  TeV with the ATLAS experiment*, ATLAS-CONF-2016-088, .

- [84] CMS collaboration, C. Collaboration, *Search for charged Higgs bosons with the  $H^\pm \rightarrow \tau^\pm \nu_\tau$  decay channel in the fully hadronic final state at  $\sqrt{s} = 13$  TeV*, *CMS-PAS-HIG-16-031*, .
- [85] ATLAS collaboration, T. A. collaboration, *Search for charged Higgs bosons in the  $H^\pm \rightarrow tb$  decay channel in pp collisions at  $\sqrt{s} = 13$  TeV using the ATLAS detector*, *ATLAS-CONF-2016-089*, .
- [86] D. Chowdhury and O. Eberhardt, *Global fits of the two-loop renormalized Two-Higgs-Doublet model with soft  $Z_2$  breaking*, *JHEP* **11** (2015) 052, [[1503.08216](#)].